



**HAL**  
open science

## Spindle-shaped archaeal viruses evolved from rod-shaped ancestors to package a larger genome

Fengbin Wang, Virginija Cvirkaite-Krupovic, Matthijn Vos, Leticia Beltran, Mark A.B. Kreutzberger, Jean-Marie Winter, Zhangli Su, Jun Liu, Stefan Schouten, Mart Krupovic, et al.

► **To cite this version:**

Fengbin Wang, Virginija Cvirkaite-Krupovic, Matthijn Vos, Leticia Beltran, Mark A.B. Kreutzberger, et al.. Spindle-shaped archaeal viruses evolved from rod-shaped ancestors to package a larger genome. Cell, 2022, 185 (8), pp.1297-1307.e11. 10.1016/j.cell.2022.02.019 . pasteur-03620791

**HAL Id: pasteur-03620791**

**<https://pasteur.hal.science/pasteur-03620791v1>**

Submitted on 26 Mar 2022

**HAL** is a multi-disciplinary open access archive for the deposit and dissemination of scientific research documents, whether they are published or not. The documents may come from teaching and research institutions in France or abroad, or from public or private research centers.

L'archive ouverte pluridisciplinaire **HAL**, est destinée au dépôt et à la diffusion de documents scientifiques de niveau recherche, publiés ou non, émanant des établissements d'enseignement et de recherche français ou étrangers, des laboratoires publics ou privés.

1  
2  
3  
4  
5  
6  
7  
8  
9  
10  
11  
12  
13  
14  
15  
16  
17  
18  
19  
20  
21  
22  
23  
24  
25  
26  
27  
28  
29  
30

Spindle-shaped archaeal viruses  
evolved from rod-shaped ancestors  
to package a larger genome

Fengbin Wang<sup>1,†</sup>, Virginija Cvirkaite-Krupovic<sup>2,†</sup>, Matthijn Vos<sup>3</sup>, Leticia C. Beltran<sup>1</sup>, Mark A.B. Kreutzberger<sup>1</sup>, Jean-Marie Winter<sup>3</sup>, Zhangli Su<sup>1</sup>, Jun Liu<sup>4</sup>, Stefan Schouten<sup>5</sup>, Mart Krupovic<sup>2,\*</sup> and Edward H. Egelman<sup>1,\*,a</sup>

<sup>1</sup>Department of Biochemistry and Molecular Genetics  
University of Virginia  
Charlottesville, VA 22903, U.S.A.

<sup>2</sup>Institut Pasteur, Université de Paris  
CNRS UMR6047, Archaeal Virology Unit, 75015 Paris, France

<sup>3</sup>NanoImaging Core Facility, Centre de Ressources et Recherches Technologiques (C2RT),  
Institut Pasteur, 75015 Paris, France

<sup>4</sup>Department of Microbial Pathogenesis & Microbial Sciences Institute,  
Yale University School of Medicine  
New Haven, CT 06510, U.S.A.

<sup>5</sup>NIOZ Royal Netherlands Institute for Sea Research  
Department of Marine Microbiology and Biogeochemistry  
Texel, The Netherlands

† These authors contributed equally to this paper

<sup>a</sup> Lead Contact

\* Correspondence to [mart.krupovic@pasteur.fr](mailto:mart.krupovic@pasteur.fr), [egelman@virginia.edu](mailto:egelman@virginia.edu)

31 **Summary**

32 Spindle- or lemon-shaped viruses infect archaea in diverse environments. Due to the highly  
33 pleomorphic nature of these virions, which can be found with cylindrical tails emanating from  
34 the spindle-shaped body, structural studies of these capsids have been challenging. We have  
35 determined the atomic structure of the capsid of Sulfolobus monocaudavirus 1, a virus that  
36 infects hosts living in nearly boiling acid. A highly hydrophobic protein, likely integrated into the  
37 host membrane before the virions assemble, forms seven strands that slide past each other in  
38 both the tails and the spindle body. We observe the discrete steps that occur as the tail tubes  
39 expand, and these are due to highly conserved quasi-equivalent interactions with neighboring  
40 subunits maintained despite significant diameter changes. Our results show how helical  
41 assemblies can vary their diameters, becoming nearly spherical to package a larger genome,  
42 and suggest how all spindle-shaped viruses have evolved from archaeal rod-like viruses.

43

44

## 45 **Introduction**

46 Capsids are a hallmark of viruses, which distinguishes them from all other types of  
47 mobile genetic elements (Forterre et al., 2014; Raoult and Forterre, 2008). Over billions of  
48 years, viruses have ‘invented’ capsids on multiple independent occasions from non-homologous  
49 and structurally unrelated proteins (Krupovic et al., 2019). Nevertheless, the majority of known  
50 viruses package their genomes into icosahedral or filamentous helical protein capsids (also  
51 called nucleocapsids if surrounded by an additional layer, e.g., lipid membrane) (Krupovic and  
52 Koonin, 2017; Sevvana et al., 2021). Viruses infecting archaea notoriously deviate from this  
53 general paradigm by producing virions with unique, odd-shaped morphologies, which are not  
54 observed among bacterial or eukaryotic viruses (Dellas et al., 2014; Prangishvili et al., 2017).  
55 Such archaea-specific virion architectures resemble droplets, champagne bottles or spindles  
56 (Baquero et al., 2020). Viruses with spindle-shaped (or lemon-shaped) virions are particularly  
57 common in diverse extreme and moderate environments and infect a wide range of archaeal  
58 lineages from the phyla Crenarchaeota, Euryarchaeota and Thaumarchaeota as well as  
59 Asgardarchaeota, a group of archaea widely considered to represent the closest archaeal  
60 relatives of eukaryotes (Medvedeva et al., 2021). Because of the broad distribution in Archaea,  
61 it has been suggested that spindle-shaped viruses were associated with the last archaeal  
62 common ancestor, and possibly, even the last universal cellular ancestor (LUCA) (Krupovic et al.,  
63 2020).

64 Based on virion characteristics and genomic relationships, most spindle-shaped viruses  
65 fall into two groups (Krupovic et al., 2014). One of the groups comprises smaller spindle-shaped  
66 viruses classified into families *Fuselloviridae* (e.g., *Sulfolobus* spindle-shaped virus 1 [SSV1]),

67 *Halspiviridae* (e.g., haloarchaeal virus His1) and *Thaspiviridae* (e.g., Nitrosopumilus spindle-  
68 shaped virus 1 [NSV1]) as well as several unclassified viruses. These viruses encode homologous  
69 major capsid proteins (MCP) containing two hydrophobic, potentially membrane-spanning  
70 domains and are extruded from the host cell through a budding-like mechanism without  
71 causing cell lysis (Kim et al., 2019; Quemin et al., 2016). Attempts to determine the structures  
72 of SSV1 (Stedman et al., 2015) and His1 (Hong et al., 2015) by cryo-EM did not yield atomic  
73 models and provided little insight into virion organization. The second group includes members  
74 of the family *Bicaudaviridae*, which have larger virions and genomes. A characteristic feature of  
75 this virus assemblage is the presence of ‘tails’ emanating from one or both pointed ends of the  
76 spindle. Notably, *Acidianus* two-tailed virus (ATV) and *Sulfolobus* monocaudavirus 1 (SMV1)  
77 have been reported to develop tails extracellularly, with the only requirement for this  
78 transformation being the incubation at temperatures close to those of the natural habitats (75-  
79 90°C) (Haring et al., 2005; Uldahl et al., 2016). It has been suggested that virus-encoded MoxR-  
80 type AAA+ ATPase and a von Willebrand domain A-containing cochaperone play an active role  
81 in this process by hydrolyzing ATP stored within the virions (Scheele et al., 2011). However, the  
82 exact mechanism underlying this virion morphogenesis outside of the host cells has not been  
83 elucidated. Other bicaudaviruses, namely, *Acidianus* tailed spindle virus (ATSV) and *Sulfolobus*  
84 *tengchongensis* spindle-shaped viruses 1 and 2 (STSV1 and STSV2, respectively) are released  
85 from the cells with tails extending from one of the virion poles and do not undergo further  
86 transformation (Erdmann et al., 2014; Hochstein et al., 2016; Xiang et al., 2005). Remarkably,  
87 upon infection, STSV2 and SMV1 block normal cell division, transforming the host cell into a  
88 giant virion-producing factory, which is up to 20 times larger compared to non-infected cells

89 (Liu et al., 2021). The soluble structural protein repeatedly identified as the major component  
90 of bicaudavirus virions (Erdmann *et al.*, 2014; Hochstein *et al.*, 2016; Prangishvili et al., 2006;  
91 Xiang *et al.*, 2005) is unrelated to that of the smaller spindle-shaped viruses from the first  
92 group, leading to the suggestion that the two groups of viruses are evolutionarily distinct  
93 (Krupovic *et al.*, 2014). The protein has been crystallized for ATV and ATSV and shows a four-  
94 helix bundle fold (Goulet et al., 2010; Hochstein et al., 2018).

95         Filamentous and spherical capsids (displaying helical and icosahedral symmetries,  
96 respectively) embody the simplest virion designs dictated by the principle of ‘genetic economy’  
97 inherent to viral genomes, whereby relatively large capsids are built from a small number of  
98 distinct protein subunits interacting with each other in a way that is identical throughout the  
99 capsid (Crick and Watson, 1956). For icosahedral viruses, Caspar and Klug proposed that  
100 interactions between the capsomers are quasi-equivalent (rather than identical) and developed  
101 the quasi-equivalence theory which allows predicting the arrangement of capsomers in larger  
102 icosahedral capsids (Caspar and Klug, 1962). How complex capsids, such as those of spindle-  
103 shaped viruses, are organized and how they have evolved remains unclear. While two  
104 theoretical models have been postulated for the geometric basis of the spindle shape in  
105 archaeal viruses (Perotti et al., 2016; Perotti et al., 2019), we show that they bear no relation to  
106 the actual structure of these viruses. Similarly, we can show that the crystal structures for the  
107 putative MCPs in both ATV (Goulet *et al.*, 2010) and ATSV (Hochstein *et al.*, 2018) were not of  
108 the MCPs, but unrelated viral proteins. Since spindle-shaped viruses appear to have evolved  
109 from archaeal rod-like viruses, our results explain why spindle-shaped viruses have thus far only  
110 been observed to infect archaea.

111  
112  
113  
114  
115  
116  
117  
118  
119  
120  
121  
122  
123  
124  
125  
126  
127  
128  
129  
130  
131  
132

## Results

Cryo-EM images of SMV1 (Figure 1A) show that the spindle-shaped body of the virion is continuous with the tubular tails extending out from the body. As observed for ATSV (Hochstein *et al.*, 2018), the periodicity in the spindle body is the same as that in the tails, strongly suggesting a seamless transition between the tails and the spindles. While this periodicity was described as  $\sim 40$  Å for ATSV (Hochstein *et al.*, 2018), we found a 29 Å periodicity in SMV1 (Figure 1A). The presence or absence of tails can be modulated by prolonged incubation at high temperatures (Haring *et al.*, 2005; Uldahl *et al.*, 2016). However, the heat-treated SMV1 population remained very heterogeneous with tails displaying variable lengths and diameters. We noticed that increase in pH from 6 to 10 results in nearly uniform transformation of spindle-shaped virions into tubular structures and is accompanied by the release of material present inside of the viral particle (Figure S1A). Fractionation of the SMV1 particles on 5-20% sucrose gradient followed by analysis of the different gradient fractions showed that the viral genome was released in the form of amorphous aggregates along with proteins present in the lumen of the viral particles, whereas tubular structures were largely devoid of DNA (Figure S1B). Thus, given that the tubular tails must have helical symmetry, and understanding the tails would reveal the structure of the more complicated spindle body, most of the structural studies in this paper were performed on the capsids which were transformed into a tubular state (see Methods). Nevertheless, extensive analysis of millions of segments revealed a nearly continuous variation in the diameter of the tail tubes. Progress was only made by starting from a dataset containing six million particles extracted from 16,401 micrographs, allowing us to use

133 multiple 2D classification cycles to find nearly homogeneous subsets of constant diameter. This  
134 classification approach showed that rather than being continuously variable, there were  
135 discrete changes in diameter. We were then able to generate three-dimensional  
136 reconstructions at a near-atomic level of resolution for 12 discrete diameters, ranging from 270  
137 to 335 Å (Figure 1B), each having a different helical symmetry, but each with seven strands  
138 (Table 1; Figure S2A). The  $\alpha$ -helices in the map had a clear hand and showed unambiguously  
139 that the seven strands were left-handed, as had been determined at low-resolution by cryo-  
140 electron tomography and sub-tomogram averaging. The resolution of the best volume (Table 1,  
141 symmetry 7,  $\sim 3.5$  Å, Figure 1C) would be more than adequate to build a full-atomic model *ab*  
142 *initio* when given the protein sequence.

143         To determine the identity of the MCP, SMV1 proteins were separated by SDS-PAGE and  
144 the major protein band of  $\sim 14$  kDa was subjected to trypsin digestion followed by mass  
145 spectrometry analysis (Figure S3). The dominant protein in the band, gp11 (W0UU99), was the  
146 homolog of the MCPs previously identified in all other bicaudaviruses (Erdmann *et al.*, 2014;  
147 Hochstein *et al.*, 2016; Prangishvili *et al.*, 2006; Xiang *et al.*, 2005). However, it was impossible  
148 to thread the sequence of this putative MCP (gp11) through the density map, trying both  
149 possible N-to-C orientations. The absence of density in the map for a bulky side chain might be  
150 explained by disorder of that residue, but no threading could account for the pattern of bulky  
151 side chains seen in the map. Further, while the atomic structures of the ATV (PDB ID: 3FAJ) and  
152 ATSV (PDB ID: 5EQW) putative MCPs each displayed a compact four-helix bundle with a short  
153 fifth helix projecting out, the SMV1 capsid protein was clearly composed of two long helices  
154 connected by a short turn. We therefore searched for other possible candidates. A  $C_\alpha$  trace of

155 the density map suggested that the MCP is ~90 amino acids long. Assuming that there might be  
156 disordered residues at either the N- or C-terminus that were not present in the density map, we  
157 focused on SMV1 proteins containing between 90 and 150 residues. There were 17 such  
158 candidates (out of 96 proteins), but none could be successfully threaded through the map.

159 We next performed the N-terminal sequencing of the proteins in the major gel band.  
160 Two different five-residue N-terminal peptides were identified: one from a minor species,  
161 VEDYF, corresponding to the N-terminus of gp11 (the putative MCP that did not fit the map),  
162 and one from the major species, VTFGT, that did not correspond to the N-terminus from any of  
163 the 96 ORFs in the SMV1 genome. A search of the ORFs, found this pentapeptide uniquely in  
164 SMV1 gp03 (W0UUV5), a hypothetical 157-residue sequence annotated as a membrane  
165 protein. Removing 59 N-terminal residues would place the pentapeptide at the N-terminus of a  
166 processed protein, and the resulting 98-residue protein fit the density map perfectly (Figure  
167 1D). The 98-residue protein contains no useful tryptic digestion sites (one at the C-terminus  
168 would create a three-residue peptide), explaining why peptides from this protein were never  
169 detected after tryptic digestion and mass spectrometry. The processing is likely performed by a  
170 cellular protease, because SMV1 and other bicaudaviruses do not encode identifiable  
171 proteases. Notably, however, gp03 does not contain a canonical signal sequence or  
172 recognizable signal peptidase cleavage site (Figure S4A). The fit revealed that additional density  
173 facing the outside of the capsid, near the turn between the two helices, was most likely due to  
174 heavy N-linked glycosylation of Asn53. Since the predicted MW for the 98-residue MCP is  
175 10.1kDa, we suggest that extensive glycosylation of this single residue can explain why the  
176 protein runs in a gel with an apparent MW of ~14kDa. The glycosylation on the outside of the

177 virion may play a role in protecting the capsid against very aggressive conditions, as was shown  
178 for extensively glycosylated pili of hyperthermophilic and acidophilic archaea (Wang et al.,  
179 2020; Wang et al., 2019). To further validate this, we used trifluoromethanesulfonic acid  
180 (TFMS), which removes both N- and O-linked glycans from proteins (Sojar and Bahl, 1987).  
181 Conditions were found under which a significant shift to lower mass could be obtained for a  
182 silver-stained band that ran at ~13 kDa before acid treatment and at ~11 kDa after acid  
183 treatment. These two bands were excised from the gel and analysed by mass spectrometry,  
184 which found that the gp03 can only be detected in the lower band. Interestingly, the protein  
185 gp11 was detected in both bands (Figure S3B-D). Thus, we designate SMV1 gp03 as the actual  
186 MCP. Given the abundance of gp11 in the virions of all known bicaudaviruses and lack of any  
187 discernable contribution to capsid formation, we hypothesize that this protein functions as a  
188 nucleocapsid protein which compacts and, potentially, protects the viral DNA. Notably, in ATV,  
189 gp42, one of the two ATV-encoded homologs of SMV1 gp11, has been shown to act as a strong  
190 inhibitor of the host RNA polymerase (Sheppard et al., 2016), consistent with the possibility  
191 that this soluble protein is injected into the cell upon viral genome delivery.

192

### 193 *Kinship among all spindle-shaped viruses*

194 We have imaged ATV by cryo-EM (Figure 2A) and carried out a similar analysis. As with  
195 SMV1, ATV is formed from 7-start helical strands, and the subunit contains two  $\alpha$ -helices linked  
196 by a short turn. The repeat of the 7-start helices in ATV is 32 Å compared with the 29 Å in  
197 SMV1. Although the resolution we have obtained for ATV (~6 Å) is much worse than for SMV1,  
198 there is no ambiguity in building a homology model for the ATV gp59 (YP\_319890) based upon

199 the SMV1 results, and this model fits well into the reconstructed density (Figure 2C). The crystal  
200 structure for the putative MCP in ATV, gp62 (PDB id: 3FAJ)(Goulet *et al.*, 2010), cannot be fitted  
201 into the density, and clearly is the structure of a different protein. Thus, we designate gp59 as  
202 the actual MCP of ATV.

203 Homologs of SMV1 gp03 and ATV gp59 are conserved in all bicaudaviruses, including  
204 STSV1 and STSV2 (Figure S4B). Based upon the results for SMV1 and ATV, everything suggests  
205 that the actual MCP of ATSV is ATSV\_F163, rather than ATSV\_D135 for which an x-ray crystal  
206 structure was determined (Hochstein *et al.*, 2018). The N-glycosylation sequon (NxS/T, where x  
207 is any amino acid) located at the beginning of the second  $\alpha$ -helix is conserved in all homologs  
208 (Figure S4B), suggesting that glycosylation is important for virion assembly and/or stability.  
209 Features of the bicaudavirus MCPs are remarkably similar to those of the MCPs of group I  
210 spindle-shaped viruses, such as fusellovirus SSV1, halspivirus His1 and thaspivirus NSV1 (Figure  
211 S4C). Notably, the MCP of SSV1 is encoded as a pre-protein which is proteolytically processed at  
212 the N-terminus (Iverson *et al.*, 2017; Quemain *et al.*, 2015), as in the case of SMV1. Furthermore,  
213 MCPs of fuselloviruses also contain the conserved N-glycosylation sites at the position  
214 equivalent to that in bicaudaviruses and SSV1 MCP has been indeed shown to be glycosylated  
215 (Quemin *et al.*, 2015). Finally, fuselloviruses, halspiviruses and thaspiviruses were all shown to  
216 exist in tubular form, either upon virion egress or following genome ejection (Hong *et al.*, 2015;  
217 Kim *et al.*, 2019; Quemain *et al.*, 2016). In light of this evidence, combined with the results of  
218 bipartite network analysis showing that bicaudaviruses and group I spindle-shaped viruses  
219 share several signature genes (Iranzo *et al.*, 2016), we suggest that all archaeal spindle-shaped  
220 viruses have evolved from a common ancestor and use similar principles of virion organization

221 (Figure 3C). However, details in both the protein subunits and the virion morphology differ, as  
222 would be expected from evolutionary divergence. For instance, viruses STSV1 and STSV2 have  
223 only one, relatively short tail and do not undergo morphological changes outside of the cell  
224 (Erdmann *et al.*, 2014; Xiang *et al.*, 2005); ATSV has a very long and narrow tail of uniform  
225 length (Hochstein *et al.*, 2018); whereas ATV and SMV1 analyzed in the present paper can  
226 “grow” tails from both pointed ends of the spindle (Haring *et al.*, 2005; Uldahl *et al.*, 2016).  
227 Strikingly, this emerging virus lineage might extend beyond spindle-shaped viruses to also  
228 include rod-shaped viruses of the family *Clavaviridae* (Mochizuki *et al.*, 2010). In particular, a  
229 high resolution experimentally-determined structure exists for a rod-like clavavirus APBV1  
230 virion (Ptchelkine *et al.*, 2017), which is constructed from highly hydrophobic subunits with a  
231 helical-hairpin structure and an N-glycosylation site at the same position as in SMV1 and other  
232 bicaudaviruses (Figure 3B). Although MCPs of APBV1 and SMV1 do not display significant  
233 sequence similarity, which is not unexpected due to high sequence divergence and sparse  
234 sampling of archaeal viruses, the interactions between the MCP subunits in the two groups of  
235 viruses are very similar, full of hydrophobic interactions (Figure 3B).

236

### 237 *How the virions expand*

238 The subunit model from “symmetry 7” of SMV1 (Figure 1D) fits the other 11 volumes  
239 with no modifications or perturbations. In addition, changes in the local packing of the subunit  
240 were almost infinitesimally small in the diameter range from 270 to 335 Å (Figure 4,  
241 Supplemental Movies 1 and 2), showing how the diameter could change significantly while at  
242 the same time preserving a highly conserved local environment for each subunit. The RMSD

243 between two adjacent subunits in the same strand comparing the smallest and the largest  
244 diameter was only 0.3 Å (Figure 4A), while the RMSD between subunits in adjacent strands was  
245 only 0.4 Å (Figure 4B) when comparing the smallest and largest diameter.

246 Helical symmetry can be defined as a rise per subunit, a rotation per subunit, and a  
247 possible  $C_n$  rotational symmetry. Two of the 12 structures had a  $C_7$  rotational symmetry (Table  
248 1, symmetries 1 and 8), so the rise per subunit in each strand is the same as the helical rise. For  
249 the other symmetries in Figure 4C we have multiplied the helical rise by seven to yield the rise  
250 per subunit within a strand. The determined diameters for these 12 points fall into a small  
251 range, considering that the spindle bodies can have a maximum diameter of ~1,200 Å. Because  
252 the 29 Å periodicity remains constant in both spindle body and tail, and this comes from the  
253 repeat of the 7-start helices which have a fixed 203 Å pitch ( $7 \times 29$  Å) in both the tails and the  
254 spindle body, the number of subunits per strand in one turn will be  $u$ , which is 203 Å divided by  
255 the rise per subunit along a strand. We have found for the 12 symmetries reconstructed that  $u$   
256 is incremented by seven for each larger diameter (which is an increment of one per 29 Å),  
257 explaining why the changes in diameter,  $D$ , are discrete, and not continuous. Let  $p$  be the path  
258 length along a 7-start strand per 203 Å turn, then:

$$259 \quad p^2 = (\pi D)^2 + 203^2$$

260 We have shown that the local packing does not change as the diameter changes (Figure  
261 4, Supplemental Movies 1,2), so the spacing between subunits along a strand,  $q$ , can be taken  
262 as a constant as the diameter changes, and  $p = uq$ . From the observed tubes,  $q=18.8$  Å. Given  
263 this, the rise per subunit and the diameter can be easily calculated for each successive value of

264 *u.* Therefore, we can extrapolate the results from the tubes to the larger diameters that would  
265 be found in the spindles (Figure 4C, Supplemental Movie 3).

266         How can the subunit structure explain the remarkable ability of these strands to slide  
267 past each other in discrete steps? An analysis of the protein sequence (Figure 5A) shows that  
268 most of the residues are quite hydrophobic. A plot of transmembrane probabilities for the  
269 sequence indicates a strong prediction for two transmembrane helices (Figure 5B). This can be  
270 seen in terms of the actual structure, where there is a hydrophobic region in the center of the  
271 subunit that is  $\sim 35$  Å thick, with polar regions below and above it (Figure 5C). Therefore, these  
272 capsid proteins would not be soluble as monomers and must be integral to the host membrane  
273 before the virions are formed. When packed into virions (Figure 5D), the hydrophobic regions  
274 are completely buried and the polar regions are facing either the outside or the lumen. Notably,  
275 the interface between neighboring 7-start strands is almost completely hydrophobic, with  
276 minimal interactions between the hydrophilic regions. This will allow these strands to slide by  
277 each other while still excluding solvent (Supplemental Movies 4,5). Consistent with this,  
278 treatment of the virions with detergent, such as N-lauryl sarcosine, leads to rupture of the  
279 virions (Figure S5A), much as such treatment would destabilize a membrane.

280         The extensive hydrophobicity of the capsid and likely insertion of the protein subunits  
281 into the membrane prior to virion assembly motivated us to look for possible lipids associated  
282 with the virions (Figure S5B). The distribution of lipids in the SMV1 virions was not the same as  
283 that found in the host, suggesting that these lipids were selectively incorporated rather than  
284 being contaminants from cellular debris. In bacterial mating pili, the subunits also have a  
285 helical-hairpin structure (Costa et al., 2016; Zheng et al., 2020) and these subunits exist as

286 integral membrane proteins before polymerization and after depolymerization. A single lipid  
287 molecule has been observed tightly bound to each subunit in the three published structures.  
288 However, we found no ordered lipid molecules in the SMV1 tube reconstructions. We can  
289 exclude the possibility that disordered lipid molecules (that we do not visualize) are present  
290 between the hydrophobic helices as the space between these helices is too narrow to  
291 accommodate a lipid. Since the tube segments used for three-dimensional reconstruction were  
292 carefully screened to only include the most ordered and regular ones, we are thus left with the  
293 possibility that the lipids may be found in the many dislocations or irregular regions in the  
294 virions, in particular, where additional subunits are added to helical turns as the diameter  
295 becomes larger. Alternatively, lipids could be associated with the specialized structures that are  
296 present at the termini of SMV1 virions.

297

298

## 299 **Discussion**

300 We have shown how a highly hydrophobic subunit can assemble into tubes with a  
301 variable diameter, and how these tubes can seamlessly expand and contract to form a spindle-  
302 shaped body for a virion that maintains the same quasi-equivalent contacts between subunits  
303 that are present in the tubes. The hydrophobic effect is, by definition, non-specific (Hillyer and  
304 Gibb, 2016; Newberry and Raines, 2019), and the hydrophobic surfaces of the helices (Figure 5)  
305 allow them to slide past each other (Supplemental Movies 4,5) while still maintaining the  
306 integrity of the capsid and excluding very acidic solvent in the environment from the interior of  
307 the virion. Our expectation is that the interior of the virions is close to the same near-neutral  
308 pH as the cytoplasm of the host (Baker-Austin and Dopson, 2007) and that is why the capsid  
309 must be impermeable to acidic solvent. While the hydrophobic effect alone is non-specific,  
310 specificity in the intersubunit contacts is provided by the helix-helix contacts that exist between  
311 neighboring subunits which dictate that discrete changes in diameter are required to maintain  
312 these quasi-equivalent contacts (Supplemental Movies 4,5). The notion of quasi-equivalence  
313 was first introduced by Caspar and Klug to explain how icosahedral viruses could be assembled  
314 from many copies of a single protein (Caspar and Klug, 1962). If one only had 60 copies of such  
315 a capsid protein a perfect icosahedron could be assembled so that every subunit was in an  
316 equivalent environment. It was also known that it was impossible to place more than 60 copies  
317 of a protein on the surface of a sphere such that all would be in strictly equivalent  
318 environments. But a capsid built from only 60 protein subunits would be quite small, and it had  
319 been observed that larger icosahedral viruses contained many more than 60 copies of the  
320 capsid protein. The solution was found in the possibility of quasi-equivalence (Caspar and Klug,

321 1962), wherein multiples of 60 protein subunits could be assembled into a spherical shell  
322 maintaining not identical, but quasi-equivalent contacts. This has now been amply confirmed  
323 with high resolution structures for many icosahedral viruses (Damodaran et al., 2002; Johnson  
324 and Olson, 2021; Johnson and Speir, 1997), although it has also been shown that certain  
325 icosahedral viruses can violate quasi-equivalence (Rayment et al., 1982; Stehle et al., 1994).  
326 However, the extension of quasi-equivalence theory to the radial expansion of helical viruses  
327 has not been envisioned.

328         Here we show that the quasi-equivalence principle explaining the ability of icosahedral  
329 viruses to expand the number of subunits needed to encapsulate larger genomes has a striking  
330 parallel in helical viruses. In APBV1 or other rod-like viruses, there will be a stoichiometric ratio  
331 between the number of capsid proteins and the number of bases or base pairs encapsidated. As  
332 pointed out by Caspar and Klug (Caspar and Klug, 1962), the length of tobacco mosaic virus  
333 virions is simply determined by the length of the single-stranded RNA genome given the  
334 stoichiometric ratio of three bases per protein subunit. In filamentous bacteriophage, the  
335 packaging of DNA involves charged residues in the lumen of the phage, and thus modifications  
336 of these residues can change the length of the virions while the length of the genome is  
337 unaltered (Hay and Lithgow, 2019). Thus, there is a linear relation between the length of the  
338 virion and the size of the genome, even though the actual stoichiometry can be modified. In  
339 contrast, for spherical viruses the number of capsid subunits will be proportional to the surface  
340 area, which is the radius squared, while the size of the genome encapsidated will scale as the  
341 radius cubed. Thus, the ratio of base pairs per capsid subunit will scale as the radius, becoming  
342 more efficient in genome packaging the larger the capsid.

343           With hydrophobic subunits having the ability to slide past each other, it is easy to  
344 imagine how a rod-like virus such as APBV1 could evolve into a spindle-shaped virus (Figure 3C)  
345 while still maintaining all of the local interactions that hold the capsid together. We suggest  
346 that the minimum energy conformation of the spindle-shaped capsids is actually a tube, as  
347 evidenced by the fact that when the genome is released, the SMV1 spindles relax into tubes  
348 (Figure S1). The same spindle-to-tube transformation has been observed upon genome ejection  
349 for a group I spindle-shaped virus His1 (Hong *et al.*, 2015). It is therefore the pressure of the  
350 genome that expands the capsid that would normally be rod-like into a spindle shape. Thus, the  
351 unusual spindle morphology results from the radial expansion of a rod.

352           Archaeal and bacterial gas vesicles (Li and Cannon, 1998; Pfeifer *et al.*, 2002; Strunk *et*  
353 *al.*, 2011) have some remarkable similarity in morphology to spindle-shaped viruses. The gas  
354 vesicles are made of a single major structural protein of ~8 kDa and have a hydrophobic interior  
355 surface. However, whereas the capsid proteins contain two hydrophobic  $\alpha$ -helices, those of gas  
356 vesicles from both bacteria and archaea have a  $\alpha$ - $\beta$ - $\beta$ - $\alpha$  structure (Knitsch *et al.*, 2017; Strunk *et*  
357 *al.*, 2011), and the  $\beta$ -strands are predicted to mediate subunit-subunit interactions. Finally,  
358 unlike the capsid proteins which are predicted to contain two transmembrane domains, the  
359 proteins of gas vesicles are predicted to have none. Thus, we conclude that the superficial  
360 similarity between spindle-shaped viruses and gas vesicles is a result of convergent evolution.  
361 However, given the hydrophobic nature of both structures, we predict that changes in diameter  
362 described for both are mediated by these hydrophobic interactions.

363           There has been great interest in understanding the role of BAR domain proteins (Frost  
364 *et al.*, 2008), ESCRT-III (Endosomal Sorting Complexes Required for Transport) (Pfitzner *et al.*,

365 2021) and dynamin family proteins (Antonny et al., 2016) in membrane remodeling. All of these  
366 proteins form helical tubes of variable diameters that have been shown to constrict as part of  
367 their role in processes such as membrane fission and vesiculation. Structural studies of these  
368 assemblies have been extremely difficult due to the variability of tube diameters, and we still  
369 do not have any models at an atomic level of detail for the elementary steps in constriction.  
370 Similarly, keratin filaments, assembled from  $\alpha$ -helical coiled-coils, have also been revealed to  
371 form variable diameter tubes *in situ* (Weber et al., 2021). While we do not suggest any  
372 homology between these proteins and the SMV1/ATV capsid proteins, we suggest that the  
373 general principle underlying the sliding of the strands of SMV1 proteins past each other while  
374 maintaining the structural integrity of the capsid might extend to other filamentous assemblies  
375 with variable diameters. The great advances in cryo-EM that have allowed us to determine in  
376 atomic detail the structure of SMV1 capsid will likely allow a similar level of understanding for  
377 other assemblies in the near future.

378

### 379 *Limitations of the Study*

380 We have determined a high resolution structure for only a single spindle-shaped virus, SMV1,  
381 and determined a lower resolution structure for a second spindle-shaped virus, ATV. These  
382 results have been combined with an existing high resolution structure for the clavavirus APBV1  
383 (Ptchelkine *et al.*, 2017) and homology models of the major capsid proteins from other spindle-  
384 shaped viruses to show the likely common ancestry and suggest how the spindle-shaped viruses  
385 have evolved from rod-like viruses such as APBV1. Future high resolution studies of other rod-  
386 like and spindle-shaped viruses will greatly extend our understanding of this evolution. Just as

387 knowing the morphology and genetics of apes and humans suggests common ancestry,  
388 determining the intermediates that existed in this evolutionary process gives one a much more  
389 profound understanding of biological history.

390  
391 **Acknowledgments**

392 We are grateful to Dr. Xu Peng (University of Copenhagen) for the kind gift of SMV1 and its  
393 host, *Saccharolobus islandicus*  $\Delta$ C1C2. Part of the cryo-EM imaging of SMV1 was done at the  
394 Molecular Electron Microscopy Core Facility at the University of Virginia, which is supported by  
395 the School of Medicine. Part of the Cryo-EM and the Cryo-ET imaging were done at the Nano-  
396 Imaging Core Facility at Institut Pasteur, created with the help of a grant from the French  
397 Government's Investissements d'Avenir program (EQUIPEX CACSICE - Centre d'analyse de  
398 systèmes complexes dans les environnements complexes, ANR-11-EQPX-0008). This work was  
399 supported by NIH Grant GM122510 (E.H.E.) and K99GM138756 (F.W.). The work in the M.K.  
400 laboratory was supported by grants from l'Agence Nationale de la Recherche (ANR-17-CE15-  
401 0005-01, ANR-20-CE20-009-02 and ANR-21-CE11-0001-01) and Ville de Paris (Emergence(s)  
402 project MEMREMA). We are grateful to Youssef Ghorbal for the help with data transfer, to  
403 Caglar Yildiz for support in the lipid analysis and to the Ultrastructural Biolmaging unit of  
404 Institut Pasteur for access to electron microscopes.

405

406

407

408 **Author Contributions**

409 M.K. initiated and developed the project. F.W. performed microscopy, image analysis,  
410 reconstructed the SMV1 and ATV tubes, and generated and refined the atomic models. V.C-K.  
411 cultured the viruses, developed the conditions for tube formation, and performed sample  
412 preparation and fractionation analyses. M.V. and J-M.W. performed microscopy. Z.S. analyzed  
413 data and developed graphical representations. L.C.B. did the deglycosylation of the MCP.  
414 M.A.B.K., M.V. and J-M.W. collected the tomographic data. J.L. analyzed the tomographic data  
415 and generated the three-dimensional reconstruction. S.S. analyzed the lipids. E.H.E. obtained  
416 funding, analyzed data and supervised the research. F.W., M.K. and E.H.E. wrote the manuscript  
417 with input from all authors.

418  
419 **Declaration of Interests**

420  
421 The authors declare no competing interests.  
422  
423

424 **Figure Legends**

425 **Figure 1. Cryo-EM of bicaudavirus SMV1**

426 **A**, Representative cryo-EM of the *Sulfolobus monocaudavirus 1* (SMV1). A 29 Å periodicity can  
427 be seen in both spindle-shaped bodies and tails. Scale bar, 50 nm.

428 **B**, Cryo-EM reconstructions of the SMV1 tails made from 12 different diameters. The top view  
429 models of the largest (symmetry 12) and smallest (symmetry 1) diameters are shown.

430 **C**, A surface of the 3.5 Å resolution reconstruction of symmetry 7. The left-handed 7-start  
431 protofilaments and 29 Å spacing between them are labeled.

432 **D**, Ribbon model of a single MCP protein (left). The map quality of the subunit is shown on the  
433 right. The arrow points to the N-linked glycosylation associated with Asn53.

434

435 **Figure 2. Cryo-EM of the *Acidianus* two-tailed virus (ATV)**

436 **A**, Representative cryo-EM of ATV. A 32 Å periodicity can be seen in both spindle-shaped bodies  
437 and tails, indicated by black arrows. Scale bar, 50 nm.

438 **B**, Surface of the cryo-EM reconstruction of the ATV tails for one diameter, with the 7-start  
439 protofilaments labeled.

440 **C**, The homology model of ATV fit into the cryo-EM map in side and top views.

441

442 **Figure 3. Spindle-shaped viruses evolved to carry larger genomes**

443 **A**, Single subunit structures of seven MCPs. The structures of the APBV1 and SMV1 MCPs have  
444 been determined by high-resolution cryo-EM (PDB 5OXE and 7ROC). The other five MCP  
445 structures are homology models based on the SMV1 structure (see Methods).

446 **B**, Comparison of hydrophobic interactions of APBV1 and SMV1.

447 **C**, The estimated internal volumes of seven viruses plotted against genome size.

448

449 **Figure 4. The local contacts between capsid subunits are conserved as the diameter changes**

450 **A**, Interactions along the 7-start protofilament. One protofilament from the tube is highlighted  
451 on the left. Two subunits in one protofilament from symmetry 1 and 12 are aligned (center) and  
452 compared (right).

453 **B**, Interactions between adjacent 7-start protofilaments. Two protofilaments are highlighted on  
454 the left. The contacts between three subunits, two on the bottom strand ( $S_a$  and  $S_b$ ) and one on  
455 the top ( $S'_a$ ) are compared in two views (center and right).

456 **C**, The rise per subunit along a strand for 12 different symmetries is plotted versus the diameter  
457 of the tubes (orange spheres), showing a nearly linear relationship. The blue dashed line shows  
458 the extrapolation to both smaller and larger diameters.

459

460 **Figure 5. The SMV1 MCP has clustered lipophilicity**

461 **A**, Amino acid composition of the SMV1 MCP.

462 **B**, TMHMM prediction of transmembrane probabilities for the SMV1 MCP sequence.

463 **C**, The spatial distribution of hydrophobic and hydrophilic residues in a single MCP.

464 **D**, Different views of the SMV1 tubes colored by lipophilicity.

465

466  
467

**Table 1. Helical symmetry and model statistics for SMV<sub>1</sub> and ATV**

Symmetry ID	SMV <sub>1</sub>												ATV
	1	2	3	4	5	6	7	8	9	10	11	12	---
<b>Helical symmetry</b>													
Point group	C7	C1	C1	C1	C1	C1	C1	C7	C1	C1	C1	C1	C1
Helical rise (Å)	5.15	0.72	0.70	0.68	0.67	0.66	0.64	4.38	0.61	0.60	0.59	0.58	1.08
Helical twist (°)	-9.0	50.2	-155.5	-104.1	101.7	153.1	-52.6	-7.7	50.4	-155.3	-103.9	101.8	-156.0
<b>Map resolution (Å)</b>													
Model:map FSC (Å, 0.5)	5.1	4.8	4.3	4.1	4.1	3.9	3.7	3.8	3.7	3.8	4.0	4.3	---
Map:map FSC (Å, 0.143)	4.4	4.3	3.8	3.8	3.8	3.8	3.7	3.7	3.4	3.5	3.6	4.0	6.3
<b>Refinement and Model validation</b>													
Bond lengths RMSD (Å)	0.004	0.004	0.006	0.005	0.006	0.004	0.003	0.004	0.006	0.007	0.005	0.004	---
Bond angles RMSD (°)	0.658	0.640	0.770	0.841	0.671	0.699	0.635	0.703	0.681	0.735	0.651	0.658	---
Clashscore	12.4	9.9	12.0	9.3	10.0	8.4	9.0	10.9	9.2	11.0	8.7	7.4	---
Ramachandran Favored (%)	96.7	95.7	94.6	95.7	94.6	95.7	93.4	95.0	93.4	94.6	94.6	95.7	---
Ramachandran Outlier (%)	0	0	0	0	0	0	0	0.2	0	0	0	0	---
RSCC	0.86	0.87	0.87	0.87	0.88	0.87	0.87	0.88	0.87	0.87	0.86	0.87	---
<b>Deposition ID</b>													
PDB (model)	7RO2	7RO3	7RO4	7RO5	7RO6	7ROB	7ROC	7ROD	7ROE	7ROG	7ROH	7ROI	---
EMDB (map)	24585	24586	24587	24588	24589	24590	24591	24592	24593	24594	24595	24597	24596

468  
469  
470

471  
472

473

474 **STAR Methods**

475

476 **RESOURCE AVAILABILITY**

477

478 **Lead Contact**

479 Further information and requests for resources and reagents should be directed to and will be

480 fulfilled by the lead contact, Edward H. Egelman, [egelman@virginia.edu](mailto:egelman@virginia.edu)

481 **Materials Availability**

482

- 483 • This study did not generate any new unique reagents.

484

485 **Data and Code Availability**

- 486 • The SMV1 maps were deposited in the Electron Microscopy Data Bank (EMDB) with  
487 entry codes EMD-24585, EMD-24586, EMD-24587, EMD-24588, EMD-24589, EMD-  
488 24590, EMD-24591, EMD-24592, EMD-24593, EMD-24594, EMD-24595, and EMD-24597  
489 and the respective atomic models were deposited in the Protein Data Bank (PDB) with  
490 entry codes 7RO2, 7RO3, 7RO4, 7RO5, 7RO6, 7ROB, 7ROC, 7ROD, 7ROE, 7ROG, 7ROH  
491 and 7ROI. The ATV map was deposited in the EMDB with entry code EMD-24596.

492

- 493 • This paper does not report original code.

494

- 495 • Any additional information required to reanalyze the data reported in this paper is  
496 available from the lead contact upon request

497

498

499

500 **EXPERIMENTAL MODEL AND SUBJECT DETAILS**

501

502 **Archaeal strains and growth conditions**

503 *Sulfolobus monocaudavirus 1*, SMV1, was propagated in *Sulfolobus islandicus* CRISPR deletion  
504 mutant delta C1C2 (Gudbergdottir et al., 2011). The host cell culture was grown in *Sulfolobus*  
505 medium supplemented with 0.2% tryptone, 0.1% yeast extract, 0.2% sucrose and 0.002% uracil  
506 (Zillig et al., 1993). The culture was started from  $-80^{\circ}\text{C}$  stock. The cells were grown in 50 ml of  
507 medium at  $76^{\circ}\text{C}$  with shaking. After 24 h of incubation, the cell culture was diluted 20 times in  
508 pre-warmed ( $76^{\circ}\text{C}$ ) medium and the growth was continued until it reached an  $\text{OD}_{600}$  of  $\sim 0.2$ .  
509 Then the cells were infected with SMV1 stock and incubation continued at  $76^{\circ}\text{C}$  with agitation  
510 for 24h. 24 h post infection the cells were removed by centrifugation in Sorval 3000 rotor, 7000  
511 rpm, 20 min,  $15^{\circ}\text{C}$ , virus-containing supernatant was collected and virions precipitated with  
512 PEG600 (10.5% w/v) and NaCl (5.8% (w/v) for 2h at room temperature. The PEG-precipitate was  
513 then pelleted in a Sorval 3000 rotor, 9000 rpm, 30 min,  $15^{\circ}\text{C}$  and the resulting pellet was re-  
514 suspended in one tenth of the original volume in 20 mM Tris-acetate (pH6) buffer.

515

516 **METHODS DETAILS**

517 **Virus production and treatments**

518 To purify the virus, solid CsCl was added to the virus suspension to a final concentration of 45%  
519 (w/v). The samples were run in a Beckman SW41 rotor, 38,000 rpm, at least 16 h,  $15^{\circ}\text{C}$ . After the  
520 run, the opalescent band corresponding to SMV1 virions was collected. The purified SMV1 was  
521 stored in CsCl at  $4^{\circ}\text{C}$  until used.

522 For SMV1 virion dissociation, CsCl purified virions were diluted 50 times in 20 mM Tris-acetate  
523 (pH6) buffer and pelleted down by centrifugation in a Beckman 45Ti rotor, 35,000 rpm, 2 h, 15°C.  
524 The resultant pellet was re-suspended in 20mM Tris-acetate (pH6) buffer and used for  
525 dissociation. The SMV1 virions were dissociated by addition of 0.1% (v/v) NaOH and incubation  
526 at 37°C for 1 h. Then non-treated (control) and NaOH-treated virions were loaded on top of the  
527 linear 5-20 % sucrose gradients and run in a Beckman SW41 rotor, 24,000 rpm, 20 min, 15°C.  
528 After the run, 12 fractions from the top of each tube were collected and analyzed in 4-12% Bis-  
529 Tris acrylamide gels. After the run the gels were stained for DNA with ethidium bromide and for  
530 proteins with InstantBlue. The contents of the collected fractions were also visualized by negative  
531 staining TEM. For that, 10 µl of the fraction of interest was adsorbed onto copper grids with  
532 carbon-coated Formvar films and negatively stained with 2.0% (w/v) uranyl acetate for 20 s. The  
533 samples were observed under a FEI Tecnai BioTwin 120 microscope operated at 120 kV.

534

### 535 **Cryo-electron microscopy and image processing**

536 The SMV1 sample was applied to glow-discharged lacey carbon grids and vitrified using a  
537 Vitrobot Mark IV (Thermo Fisher). Grids were imaged at on a Titan Krios (300 keV, Thermo  
538 Fisher) with a K3 camera (Gatan). 16,401 micrographs were collected under electron counting  
539 mode at 1.1 Å per pixel, using a defocus range of 1–2 µm with ~50 electrons/Å<sup>2</sup> distributed into  
540 40 fractions. Motion correction and CTF estimation were done in cryoSPARC (Punjani et al.,  
541 2017; Rohou and Grigorieff, 2015; Zheng et al., 2017). A total of seven million particles were  
542 auto-picked by “Filament Tracer” with a shift of 13 pixel, and non-virion bad particles were  
543 removed by 2D classification. About six million SMV1 particles remained having a range of

544 diameters. From this six million particle dataset, 12 relatively homogeneous subsets were  
545 sorted out by iterative 2D classifications. The possible helical symmetries were calculated from  
546 an averaged power spectrum for each subset, generated from the raw particles. For each  
547 subset, the actual helical symmetry was determined in cryoSPARC by trial and error, until the  
548 hand of  $\alpha$ -helices and amino acid side chains were seen (Egelman, 2000; Punjani et al., 2020).  
549 The resolution of each reconstruction was estimated by both Map:Map FSC and Model:Map  
550 FSC. The final volumes were then sharpened with a negative B-factor automatically estimated  
551 in cryoSPARC, and the statistics are listed in Table 1.  
552 For ATV the same approach was used, with 2.8M particle images collected using a shift of 9  
553 pixels between adjacent boxes.

554

#### 555 **Model building of SMV1 MCP**

556 The density corresponding to a single SMV1 MCP was segmented from the experimental cryo-  
557 EM density using Chimera (Pettersen et al., 2004). Possible MCP sequences were threaded  
558 through the density using DeepTracer (Pfab et al., 2021). Only one sequence, W0UUV5, also  
559 detected by N-terminal sequencing, could be threaded through the map, matching the bulky  
560 side chain densities and the glycosylation site. This model was adjusted manually in Coot  
561 (Emsley and Cowtan, 2004) and real-space refined in PHENIX (Afonine et al., 2018). Using the  
562 determined helical symmetry, a filament model was generated in Chimera and refined against  
563 the full cryo-EM map using PHENIX real-space refinement. MolProbity was used to evaluate the  
564 quality of the filament model (Williams et al., 2018). The refinement statistics are shown in  
565 Table 1.

566

567 **Cryo-electron tomography**

568 For cryo-electron tomography, CsCl-purified virions were pelleted by ultracentrifugation  
569 (Beckman Type 50.2 Ti rotor, 32000 rpm, 2h, 15 °C), resuspended in water and incubated at 90  
570 °C for one week. Heat-treated SMV1 particles were mixed with CsCl-purified rudivirus SIRV2 as  
571 a control, since the helical hand had been determined previously (DiMaio et al., 2015). Data  
572 were collected on a Titan Krios microscope (TFS) operating at 300kV in EFTEM mode using a  
573 bioquatum/K3 (Gatan) energy filter and camera with a 20 eV slit. Tilt series were recorded at a  
574 magnification of 26kx corresponding to 3.4 Å/pixel. A tilt range of +/-60° was set with a 3° tilt  
575 increment and a total dose of 120 e<sup>-</sup>/Å<sup>2</sup> with a dose symmetric tilting scheme using the TFS  
576 tomography software with defocus values between -4 and -6 micron defocus.

577         A total of 935 segments were manually picked along the long tails of SMV1 from 8×  
578 binned tomograms by “tomopick” in the tomography package i3 (Winkler, 2007). Sub-  
579 tomograms of SMV1 were first extracted from the 8× binned tomograms, and then aligned in  
580 the i3 software package. After initial alignment, sub-tomograms were extracted from unbinned  
581 tomograms for further refinement. Multivariate statistical analysis (MSA) implemented in the I3  
582 package was then used for 3D classification and sub-tomogram averaging. As a control, a total  
583 of 200 segments were manually picked from the tubes of SMV2 from the same 8× binned  
584 tomograms. The similar procedure was used to generate a 3D averaged structure of the SIRV2  
585 tube without applying any helical symmetry. The averaged structure of SMV1 is a left-handed  
586 helix with ~29 Å periodicity, while the averaged structure of SIRV2 is a right-handed helix with  
587 ~43 Å periodicity.

588

589 **Homology modeling of ATV, SSV1, His1 and ATSV MCP**

590 The MCP homologs in bicaudaviruses were identified by PSI-BLAST (Altschul et al., 1997)  
591 searches (E-value cutoff of 0.05) queried with the sequence of SMV1 MCP (YP\_009008070)  
592 against the NCBI protein database restricted to members of the family *Bicaudaviridae*  
593 (taxid:423358). The sequences were aligned using PROMALS3D (Pei and Grishin, 2014). MCPs of  
594 SSV1 and His1 were determined experimentally (Pietila et al., 2013; Queminn *et al.*, 2015). The  
595 MCP structures of ATV, SSV1, His1 and ATSV were first predicted by AlphaFold2 (Jumper et al.,  
596 2021). Then the predicted structures were flexibly aligned to SMV1 by FATCAT (Li et al., 2020).  
597 For ATV, the predicted MCP structure was then docked into the 6 Å resolution cryo-EM map  
598 and real-space refined in PHENIX (Afonine *et al.*, 2018) with helical symmetry imposed.

599

600 **N-terminal sequencing of SMV1 by Edman Degradation**

601 The analysis was performed on an ABI Procise 494 sequencer. The sample was placed on a  
602 PVDF membrane for the Edman degradation with a cyclic procedure where residues were  
603 cleaved off one at a time and identified by chromatography. There were three steps in each  
604 cycle. In step 1 the PITC reagent was coupled to the N-terminal amino group under alkaline  
605 conditions. In step 2 the N-terminal residue was cleaved in acidic media. In step 3, the PITC-  
606 coupled residue was transferred to a flask, converted to a PTH-residue and identified by HPLC  
607 chromatography. The cycle was then started again for the identification of the next N-terminal  
608 residue.

609

610 **SMV1 deglycosylation reaction and tandem mass spectrometry**

611 Briefly, 50  $\mu$ l of concentrated SMV1 were lyophilized. Then, 150  $\mu$ l of TFMS was added to the  
612 tube and the mixture was incubated at 4 °C for 24 h. Following this, 150  $\mu$ l of 60% pyridine  
613 solution, cooled to ~15 °C with a methanol dry ice bath, was added to the reaction tube,  
614 neutralizing the TFMS acid. Using a Slide-A-Lyzer dialysis cassette with a 2,000 Da protein  
615 molecular weight cut-off (Thermo Fisher Scientific), the reaction solutions were removed from  
616 the sample with overnight dialysis at 4 °C into Tris/HCl (pH 8) buffer. After dialysis, small  
617 amounts of aggregates—presumably deglycosylated SMV1—were observed in the cassette.  
618 Centrifugation for 15 min at 4 °C and 20,000  $\times g$  was used to pellet the aggregates. The pellet  
619 was resuspended with 50  $\mu$ l of Tris buffer (pH 8). SDS-PAGE was then performed at a constant  
620 voltage of 120 V using 16.5% precast polyacrylamide Mini-PROTEAN Tris-Tricine precast gels  
621 (Bio-Rad) and Tris/Tricine/SDS running buffer (Bio-Rad). For each sample, 15  $\mu$ l of boiled sample  
622 in SDS was added to separate wells in the gel, and 5  $\mu$ l of Precision Plus Protein Dual Xtra  
623 protein standard (Bio-Rad) was used as a marker. Silver staining was performed using a Pierce  
624 Silver Stain for Mass Spectrometry kit (Thermo Fisher Scientific). The detected gel bands were  
625 then excised, and mass spectrometry (Alphalyse) was performed to analyze the composition of  
626 each band. The protein samples were reduced and alkylated with iodoacetamide, and  
627 subsequently digested with chymotrypsin. The resulting peptides were concentrated by Speed  
628 Vac lyophilization. The peptides were dissolved in 0.1% formic acid and injected on a Dionex  
629 Ultimate 3000 nano-LC system (Thermo Scientific) coupled to a Bruker Maxis Impact QTOF mass  
630 spectrometer for MS/MS analysis. Each sample underwent a 30-minute-long gradient run on  
631 the instruments. As an external control of the instrument, tryptic BSA was analysed together

632 with the samples. The results were run against the Sulfolobus monocaudavirus SMV1 proteins  
633 from the UniProt.

634

635 **Analysis of SMV1 and host cell lipids**

636 For lipid analyses, CsCl-purified virions were pelleted by ultracentrifugation (Beckman Type 50.2  
637 Ti rotor, 35000 rpm, 2h, 15 °C), resuspended in 20 mM Tris-acetate (pH6) and run on 5-20 %  
638 (wt/vol) sucrose gradient (Beckman SW32 Ti rotor, 24000 rpm, 30 min, 15 °C). The opalescent  
639 virus-containing band was collected, pelleted as above and resuspended in 20 mM Tris-acetate  
640 (pH6). The cellular and viral lipids were analyzed by UHPLC-MSD at NIOZ using an Agilent 1290  
641 Infinity II ultra-high performance LC coupled to a 6230 Agilent MSD in selected ion mode as  
642 described (Besseling et al., 2020).

643

644

645

646 **Supplemental Figures**

647

648 **Figure S1. Related to Figure 1. The pH shift to induce SMV1 to form long tails**

649 **A**, Cryo-EM of SMV1 before and after the NaOH (pH=10) treatment. Scale bars are 50 nm. The  
650 arrow indicates a tube containing a viral genome, while all of the other tubes in this image are  
651 empty.

652 **B**, SDS-PAGE and negative staining analysis of different fractions from the 5-20% sucrose  
653 gradient which were loaded with non-treated virus (left) and NaOH-treated virus (right). The  
654 non-treated virus migrated to the bottom of the gradient, where most of the protein and DNA  
655 were found (fractions 8-12), whereas following NaOH treatment, the viral DNA was found in  
656 fraction 1 in the form of amorphous aggregates, and the virion tubes were enriched in fraction  
657 3.

658

659 **Figure S2. Related to Figure 1 and Table 1. Cryo-EM volumes and helical symmetries for all 12**  
660 **reconstructions of SMV1**

661 **A**, The symmetry ID, helical rise, helical twist and point group symmetry are labeled.

662 **B**, The “gold-standard” half map FSCs were calculated in cryoSPARC using a 0.143 criterion.

663

664 **Figure S3. Related to Figure 1. TFMS deglycosylation analysis of SMV1**

665 **A**, SDS-PAGE with Coomassie blue staining of SMV1. The MW marker lane M is labeled on the  
666 left. A single band at ~ 13-14 kDa is observed for SMV1.

667 **B**, SMV1 samples on silver-stained SDS-PAGE before and after deglycosylation using TFMS. M  
668 indicates the molecular weight markers lane.

669 **C**, The band indicated by blue arrowhead in (B) was cut and used for tandem mass  
670 spectrometry analysis. Protein W0UU99 was detected.

671 **D**, The band indicated by red arrowhead in (B) was cut and used for tandem mass spectrometry  
672 analysis. Both W0UU99 and the correct capsid protein, W0UUv5, were detected.

673

674 **Figure S4. Related to Figure 3. Sequence analysis and alignments**

675 **A**, SignalP (Almagro Armenteros et al., 2019) analysis did not reveal any signal peptides or signal  
676 peptidase cleavage sites in the cleaved N-terminus.

677 **B**, The N-terminal regions which are processed in the mature proteins are not shown. The start  
678 site experimentally determined for SMV1 is indicated with an arrowhead. The secondary  
679 structure determined for the SMV1 protein is shown above the alignment, with the red ribbon  
680 representing  $\alpha$ -helices. The N-glycosylation seqon is boxed, with the target Asn residue  
681 indicated with an asterisk. Each sequence is identified with the corresponding GenBank  
682 accession number followed by the virus name.

683 **C**, The predictions of transmembrane helices within the MCPs of seven viruses were made using  
684 the TMHMM server v2.0.

685

686 **Figure S5. Related to Figure 5. Sensitivity to detergent and presence of lipids in SMV1 virions**

687 **A**, Transmission electron micrographs of negatively stained SMV1 virions treated with 0.1% N-  
688 lauryl sarcosine. Bars, 200 nm. **B**, Distribution of the lipid species identified in SMV1 host,

689 *Saccharolobus islandicus*, and SMV1 virions. GDGT, glycerol dibiphytanyl glycerol tetraether  
690 lipids; GTGT, glycerol tribiphytanyl glycerol tetraether lipids. Numbers following GDGT or GTGT  
691 represent the number of cyclopentane rings present in the lipid species.  
692  
693

694 **Supplementary Movie 1. Related to Figure 4.**

695

696 An alignment of one subunit (yellow) between two adjacent diameters: symmetry 7 (cyan) and  
697 symmetry 8 (magenta).

698

699 **Supplementary Movie 2. Related to Figure 4.**

700

701 An alignment of one subunit (yellow) between two very different diameters: symmetry 2  
702 (orange) and symmetry 12 (green).

703

704 **Supplementary Movie 3. Related to Figure 4.**

705

706 The helical symmetry established for the tubes and extrapolated to the spindle-shaped bodies  
707 (Fig. 4C) has been used to construct a model for the full capsid. The seven strands of subunits  
708 are each shown in a different color. Although discrete subunits are not seen in this visualization,  
709 98,000 copies of the capsid protein have been used to generate this model. The basis of the  
710 model is that the local packing throughout the structure is fixed with a spacing of 2.7 Å  
711 between subunits along a strand, and the helical pitch of each strand is also fixed at 203 Å. As  
712 the diameter increases due to internal pressure from the packaged genome, the strands slide  
713 past each other.

714

715 **Supplementary Movie 4. Related to Figure 5.**

716

717 The role of hydrophobic (lipophilic) surfaces in the sliding of SMV1 strands past each other. This  
718 animation shows the continuous transformation of the same number of total subunits from the  
719 narrowest diameter tube to the widest diameter tube of the 12 that we have reconstructed. As  
720 the tube becomes wider, more subunits are added per turn to the left-handed 7-start helices.  
721 The hydrophobic surfaces (gold) at the interfaces between the strands allow for this sliding to  
722 take place, at the same time that solvent is excluded from passing through the capsid.

723

724 **Supplementary Movie 5. Related to Figure 5.**

725 The top view of Supplemental movie 4.

726

727 **References**

728 Afonine, P.V., Poon, B.K., Read, R.J., Sobolev, O.V., Terwilliger, T.C., Urzhumtsev, A., and Adams,  
729 P.D. (2018). Real-space refinement in PHENIX for cryo-EM and crystallography. *Acta Crystallogr*  
730 *D Struct Biol* 74, 531-544. 10.1107/S2059798318006551.

731 Almagro Armenteros, J.J., Tsirigos, K.D., Sonderby, C.K., Petersen, T.N., Winther, O., Brunak, S.,  
732 von Heijne, G., and Nielsen, H. (2019). SignalP 5.0 improves signal peptide predictions using  
733 deep neural networks. *Nat Biotechnol* 37, 420-423. 10.1038/s41587-019-0036-z.

734 Altschul, S.F., Madden, T.L., Schaffer, A.A., Zhang, J., Zhang, Z., Miller, W., and Lipman, D.J.  
735 (1997). Gapped BLAST and PSI-BLAST: a new generation of protein database search programs.  
736 *Nucleic Acids Res* 25, 3389-3402.

737 Antonny, B., Burd, C., De Camilli, P., Chen, E., Daumke, O., Faelber, K., Ford, M., Frolov, V.A.,  
738 Frost, A., Hinshaw, J.E., et al. (2016). Membrane fission by dynamin: what we know and what  
739 we need to know. *EMBO J* 35, 2270-2284. 10.15252/embj.201694613.

740 Baker-Austin, C., and Dopson, M. (2007). Life in acid: pH homeostasis in acidophiles. *Trends in*  
741 *microbiology* 15, 165-171. 10.1016/j.tim.2007.02.005.

742 Baquero, D.P., Liu, Y., Wang, F., Egelman, E.H., Prangishvili, D., and Krupovic, M. (2020).  
743 Structure and assembly of archaeal viruses. *Advances in virus research* 108, 127-164.  
744 10.1016/bs.aivir.2020.09.004.

745 Besseling, M.A., Hopmans, E.C., Bale, N.J., Schouten, S., Damste, J.S.S., and Villanueva, L. (2020).  
746 The absence of intact polar lipid-derived GDGTs in marine waters dominated by Marine Group  
747 II: Implications for lipid biosynthesis in Archaea. *Sci Rep* 10, 294. 10.1038/s41598-019-57035-0.

748 Caspar, D.L., and Klug, A. (1962). Physical principles in the construction of regular viruses. *Cold*  
749 *Spring Harb. Symp. Quant. Biol.* 27, 1-24.

750 Costa, T.R., Ilangovan, A., Ukleja, M., Redzej, A., Santini, J.M., Smith, T.K., Egelman, E.H., and  
751 Waksman, G. (2016). Structure of the Bacterial Sex F Pilus Reveals an Assembly of a  
752 Stoichiometric Protein-Phospholipid Complex. *Cell* 166, 1436-1444 e1410.  
753 10.1016/j.cell.2016.08.025.

754 Crick, F.H., and Watson, J.D. (1956). Structure of small viruses. *Nature* 177, 473-475.  
755 10.1038/177473a0.

756 Damodaran, K.V., Reddy, V.S., Johnson, J.E., and Brooks, C.L., 3rd (2002). A general method to  
757 quantify quasi-equivalence in icosahedral viruses. *J. Mol. Biol.* 324, 723-737. 10.1016/s0022-  
758 2836(02)01138-5.

759 Dellas, N., Snyder, J.C., Bolduc, B., and Young, M.J. (2014). Archaeal Viruses: Diversity,  
760 Replication, and Structure. *Annu Rev Virol* 1, 399-426. 10.1146/annurev-virology-031413-  
761 085357.

762 DiMaio, F., Yu, X., Rensen, E., Krupovic, M., Prangishvili, D., and Egelman, E.H. (2015). *Virology*.  
763 A virus that infects a hyperthermophile encapsidates A-form DNA. *Science* 348, 914-917.  
764 10.1126/science.aaa4181.

765 Egelman, E.H. (2000). A robust algorithm for the reconstruction of helical filaments using single-  
766 particle methods. *Ultramicroscopy* 85, 225-234.

767 Emsley, P., and Cowtan, K. (2004). Coot: model-building tools for molecular graphics. *Acta*  
768 *Crystallogr.D.Biol.Crystallogr.* 60, 2126-2132.

769 Erdmann, S., Chen, B., Huang, X., Deng, L., Liu, C., Shah, S.A., Le Moine Bauer, S., Sobrino, C.L.,  
770 Wang, H., Wei, Y., et al. (2014). A novel single-tailed fusiform *Sulfolobus* virus STSV2 infecting  
771 model *Sulfolobus* species. *Extremophiles* 18, 51-60. 10.1007/s00792-013-0591-z.

772 Forterre, P., Krupovic, M., and Prangishvili, D. (2014). Cellular domains and viral lineages.  
773 *Trends in microbiology* 22, 554-558. 10.1016/j.tim.2014.07.004.

774 Frost, A., Perera, R., Roux, A., Spasov, K., Destaing, O., Egelman, E.H., De, C.P., and Unger, V.M.  
775 (2008). Structural basis of membrane invagination by F-BAR domains. *Cell* 132, 807-817.

776 Goulet, A., Vestergaard, G., Felisberto-Rodrigues, C., Campanacci, V., Garrett, R.A., Cambillau,  
777 C., and Ortiz-Lombardia, M. (2010). Getting the best out of long-wavelength X-rays: de novo  
778 chlorine/sulfur SAD phasing of a structural protein from ATV. *Acta crystallographica. Section D,*  
779 *Biological crystallography* 66, 304-308. 10.1107/S0907444909051798.

780 Gudbergsdottir, S., Deng, L., Chen, Z., Jensen, J.V., Jensen, L.R., She, Q., and Garrett, R.A. (2011).  
781 Dynamic properties of the *Sulfolobus* CRISPR/Cas and CRISPR/Cmr systems when challenged  
782 with vector-borne viral and plasmid genes and protospacers. *Mol Microbiol* 79, 35-49.  
783 10.1111/j.1365-2958.2010.07452.x.

784 Haring, M., Vestergaard, G., Rachel, R., Chen, L., Garrett, R.A., and Prangishvili, D. (2005).  
785 Virology: independent virus development outside a host. *Nature* 436, 1101-1102.  
786 10.1038/4361101a.

787 Hay, I.D., and Lithgow, T. (2019). Filamentous phages: masters of a microbial sharing economy.  
788 *EMBO reports* 20. 10.15252/embr.201847427.

789 Hillyer, M.B., and Gibb, B.C. (2016). Molecular Shape and the Hydrophobic Effect. *Annu Rev*  
790 *Phys Chem* 67, 307-329. 10.1146/annurev-physchem-040215-112316.

791 Hochstein, R., Bollschweiler, D., Dharmavaram, S., Lintner, N.G., Plitzko, J.M., Bruinsma, R.,  
792 Engelhardt, H., Young, M.J., Klug, W.S., and Lawrence, C.M. (2018). Structural studies of  
793 *Acidianus* tailed spindle virus reveal a structural paradigm used in the assembly of spindle-  
794 shaped viruses. *Proc. Natl. Acad. Sci. U.S.A.* 115, 2120-2125. 10.1073/pnas.1719180115.

795 Hochstein, R.A., Amenabar, M.J., Munson-McGee, J.H., Boyd, E.S., and Young, M.J. (2016).  
796 *Acidianus* Tailed Spindle Virus: a New Archaeal Large Tailed Spindle Virus Discovered by  
797 Culture-Independent Methods. *J Virol* 90, 3458-3468. 10.1128/JVI.03098-15.

798 Hong, C., Pietila, M.K., Fu, C.J., Schmid, M.F., Bamford, D.H., and Chiu, W. (2015). Lemon-  
799 shaped halo archaeal virus His1 with uniform tail but variable capsid structure. *Proc. Natl. Acad.*  
800 *Sci. U.S.A.* 112, 2449-2454. 10.1073/pnas.1425008112.

801 Iranzo, J., Koonin, E.V., Prangishvili, D., and Krupovic, M. (2016). Bipartite Network Analysis of  
802 the Archaeal Virosphere: Evolutionary Connections between Viruses and Capsidless Mobile  
803 Elements. *J Virol* 90, 11043-11055. 10.1128/JVI.01622-16.

804 Iverson, E.A., Goodman, D.A., Gorchels, M.E., and Stedman, K.M. (2017). Genetic Analysis of the  
805 Major Capsid Protein of the Archaeal Fusellovirus SSV1: Mutational Flexibility and  
806 Conformational Change. *Genes (Basel)* 8. 10.3390/genes8120373.

807 Johnson, J.E., and Olson, A.J. (2021). Icosahedral virus structures and the protein data bank. *J*  
808 *Biol Chem* 296, 100554. 10.1016/j.jbc.2021.100554.

809 Johnson, J.E., and Speir, J.A. (1997). Quasi-equivalent viruses: a paradigm for protein  
810 assemblies. *J. Mol. Biol.* 269, 665-675. 10.1006/jmbi.1997.1068.

811 Jumper, J., Evans, R., Pritzel, A., Green, T., Figurnov, M., Ronneberger, O., Tunyasuvunakool, K.,  
812 Bates, R., Zidek, A., Potapenko, A., et al. (2021). Highly accurate protein structure prediction  
813 with AlphaFold. *Nature*. 10.1038/s41586-021-03819-2.

814 Kim, J.G., Kim, S.J., Cvirkaite-Krupovic, V., Yu, W.J., Gwak, J.H., Lopez-Perez, M., Rodriguez-  
815 Valera, F., Krupovic, M., Cho, J.C., and Rhee, S.K. (2019). Spindle-shaped viruses infect marine  
816 ammonia-oxidizing thaumarchaea. *Proc. Natl. Acad. Sci. U.S.A.* 116, 15645-15650.  
817 10.1073/pnas.1905682116.

818 Knitsch, R., Schneefeld, M., Weitzel, K., and Pfeifer, F. (2017). Mutations in the major gas vesicle  
819 protein GvpA and impacts on gas vesicle formation in *Haloferax volcanii*. *Mol Microbiol* 106,  
820 530-542. 10.1111/mmi.13833.

821 Krupovic, M., Dolja, V.V., and Koonin, E.V. (2019). Origin of viruses: primordial replicators  
822 recruiting capsids from hosts. *Nature reviews. Microbiology* 17, 449-458. 10.1038/s41579-019-  
823 0205-6.

824 Krupovic, M., Dolja, V.V., and Koonin, E.V. (2020). The LUCA and its complex virome. Nature  
825 reviews. Microbiology 18, 661-670. 10.1038/s41579-020-0408-x.

826 Krupovic, M., and Koonin, E.V. (2017). Multiple origins of viral capsid proteins from cellular  
827 ancestors. Proc. Natl. Acad. Sci. U.S.A. 114, E2401-E2410. 10.1073/pnas.1621061114.

828 Krupovic, M., Quemin, E.R., Bamford, D.H., Forterre, P., and Prangishvili, D. (2014). Unification  
829 of the globally distributed spindle-shaped viruses of the Archaea. J Virol 88, 2354-2358.  
830 10.1128/JVI.02941-13.

831 Li, N., and Cannon, M.C. (1998). Gas vesicle genes identified in *Bacillus megaterium* and  
832 functional expression in *Escherichia coli*. Journal of bacteriology 180, 2450-2458.

833 Li, Z., Jaroszewski, L., Iyer, M., Sedova, M., and Godzik, A. (2020). FATCAT 2.0: towards a better  
834 understanding of the structural diversity of proteins. Nucleic Acids Res 48, W60-W64.  
835 10.1093/nar/gkaa443.

836 Liu, J., Cvirkaite-Krupovic, V., Baquero, D.P., Yang, Y., Zhang, Q., Shen, Y., and Krupovic, M.  
837 (2021). Virus-induced cell gigantism and asymmetric cell division in archaea. Proc. Natl. Acad.  
838 Sci. U.S.A. 118. 10.1073/pnas.2022578118.

839 Medvedeva, S., Sun, J., Yutin, N., Koonin, E.V., Nunoura, T., Rinke, C., and Krupovic, M. (2021).  
840 Viruses of Asgard archaea. bioRxiv, 2021.2007.2029.453957. 10.1101/2021.07.29.453957.

841 Mochizuki, T., Yoshida, T., Tanaka, R., Forterre, P., Sako, Y., and Prangishvili, D. (2010). Diversity  
842 of viruses of the hyperthermophilic archaeal genus Aeropyrum, and isolation of the Aeropyrum

843    pernix bacilliform virus 1, APBV1, the first representative of the family *Clavaviridae*. *Virology*  
844    402, 347-354. 10.1016/j.virol.2010.03.046.

845    Newberry, R.W., and Raines, R.T. (2019). Secondary Forces in Protein Folding. *ACS Chem Biol*  
846    14, 1677-1686. 10.1021/acscchembio.9b00339.

847    Pei, J., and Grishin, N.V. (2014). PROMALS3D: multiple protein sequence alignment enhanced  
848    with evolutionary and three-dimensional structural information. *Methods Mol Biol* 1079, 263-  
849    271. 10.1007/978-1-62703-646-7\_17.

850    Perotti, L.E., Dharmavaram, S., Klug, W.S., Marian, J., Rudnick, J., and Bruinsma, R.F. (2016).  
851    Useful scars: Physics of the capsids of archaeal viruses. *Phys Rev E* 94, 012404.  
852    10.1103/PhysRevE.94.012404.

853    Perotti, L.E., Zhang, K., Rudnick, J., and Bruinsma, R.F. (2019). Kirigami and the Caspar-Klug  
854    construction for viral shells with negative Gauss curvature. *Phys Rev E* 99, 022413.  
855    10.1103/PhysRevE.99.022413.

856    Pettersen, E.F., Goddard, T.D., Huang, C.C., Couch, G.S., Greenblatt, D.M., Meng, E.C., and  
857    Ferrin, T.E. (2004). UCSF Chimera--a visualization system for exploratory research and analysis.  
858    *J.Comput.Chem.* 25, 1605-1612.

859    Pfab, J., Phan, N.M., and Si, D. (2021). DeepTracer for fast de novo cryo-EM protein structure  
860    modeling and special studies on CoV-related complexes. *Proc. Natl. Acad. Sci. U.S.A.* 118.  
861    10.1073/pnas.2017525118.

862 Pfeifer, F., Gregor, D., Hofacker, A., Pl  $\check{d}$ sser, P., and Zimmermann, P. (2002). Regulation of gas  
863 vesicle formation in halophilic archaea. *J. Mol. Microbiol. Biotechnol.* *4*, 175-181.

864 Pfitzner, A.K., Moser von Filseck, J., and Roux, A. (2021). Principles of membrane remodeling by  
865 dynamic ESCRT-III polymers. *Trends in cell biology.* 10.1016/j.tcb.2021.04.005.

866 Pietila, M.K., Atanasova, N.S., Oksanen, H.M., and Bamford, D.H. (2013). Modified coat protein  
867 forms the flexible spindle-shaped virion of haloarchaeal virus His1. *Environmental microbiology*  
868 *15*, 1674-1686. 10.1111/1462-2920.12030.

869 Prangishvili, D., Bamford, D.H., Forterre, P., Iranzo, J., Koonin, E.V., and Krupovic, M. (2017). The  
870 enigmatic archaeal virosphere. *Nature reviews. Microbiology* *15*, 724-739.  
871 10.1038/nrmicro.2017.125.

872 Prangishvili, D., Vestergaard, G., Haring, M., Aramayo, R., Basta, T., Rachel, R., and Garrett, R.A.  
873 (2006). Structural and genomic properties of the hyperthermophilic archaeal virus ATV with an  
874 extracellular stage of the reproductive cycle. *J. Mol. Biol.* *359*, 1203-1216.  
875 10.1016/j.jmb.2006.04.027.

876 Ptchelkine, D., Gillum, A., Mochizuki, T., Lucas-Staat, S., Liu, Y., Krupovic, M., Phillips, S.E.V.,  
877 Prangishvili, D., and Huiskonen, J.T. (2017). Unique architecture of thermophilic archaeal virus  
878 APBV1 and its genome packaging. *Nat. Commun.* *8*, 1436. 10.1038/s41467-017-01668-0.

879 Punjani, A., Rubinstein, J.L., Fleet, D.J., and Brubaker, M.A. (2017). cryoSPARC: algorithms for  
880 rapid unsupervised cryo-EM structure determination. *Nat. Methods* *14*, 290-296.  
881 10.1038/nmeth.4169.

882 Punjani, A., Zhang, H., and Fleet, D.J. (2020). Non-uniform refinement: adaptive regularization  
883 improves single-particle cryo-EM reconstruction. *Nat. Methods* 17, 1214-1221.  
884 10.1038/s41592-020-00990-8.

885 Quemin, E.R., Chlanda, P., Sachse, M., Forterre, P., Prangishvili, D., and Krupovic, M. (2016).  
886 Eukaryotic-Like Virus Budding in Archaea. *mBio* 7. 10.1128/mBio.01439-16.

887 Quemin, E.R., Pietila, M.K., Oksanen, H.M., Forterre, P., Rijpstra, W.I., Schouten, S., Bamford,  
888 D.H., Prangishvili, D., and Krupovic, M. (2015). Sulfolobus Spindle-Shaped Virus 1 Contains  
889 Glycosylated Capsid Proteins, a Cellular Chromatin Protein, and Host-Derived Lipids. *J Virol* 89,  
890 11681-11691. 10.1128/JVI.02270-15.

891 Raoult, D., and Forterre, P. (2008). Redefining viruses: lessons from Mimivirus. *Nature reviews.*  
892 *Microbiology* 6, 315-319. 10.1038/nrmicro1858.

893 Rayment, I., Baker, T.S., Caspar, D.L., and Murakami, W.T. (1982). Polyoma virus capsid  
894 structure at 22.5 Å resolution. *Nature* 295, 110-115. 10.1038/295110a0.

895 Rohou, A., and Grigorieff, N. (2015). CTFFIND4: Fast and accurate defocus estimation from  
896 electron micrographs. *J. Struct. Biol.* 192, 216-221. 10.1016/j.jsb.2015.08.008.

897 Scheele, U., Erdmann, S., Ungewickell, E.J., Felisberto-Rodrigues, C., Ortiz-Lombardia, M., and  
898 Garrett, R.A. (2011). Chaperone role for proteins p618 and p892 in the extracellular tail  
899 development of *Acidianus* two-tailed virus. *J Virol* 85, 4812-4821. 10.1128/JVI.00072-11.

900 Sevvana, M., Klose, T., and Rossmann, M.G. (2021). Principles of Virus Structure. Encyclopedia  
901 of Virology, 257-277. 10.1016/B978-0-12-814515-9.00033-3.

902 Sheppard, C., Blombach, F., Belsom, A., Schulz, S., Daviter, T., Smollett, K., Mahieu, E., Erdmann,  
903 S., Tinnefeld, P., Garrett, R., et al. (2016). Repression of RNA polymerase by the archaeo-viral  
904 regulator ORF145/RIP. Nat. Commun. 7, 13595. 10.1038/ncomms13595.

905 Sojar, H.T., and Bahl, O.P. (1987). Chemical deglycosylation of glycoproteins. Meth. Enzymol.  
906 138, 341-350.

907 Stedman, K.M., DeYoung, M., Saha, M., Sherman, M.B., and Morais, M.C. (2015). Structural  
908 insights into the architecture of the hyperthermophilic Fusellovirus SSV1. Virology 474, 105-  
909 109. 10.1016/j.virol.2014.10.014.

910 Stehle, T., Yan, Y., Benjamin, T.L., and Harrison, S.C. (1994). Structure of murine polyomavirus  
911 complexed with an oligosaccharide receptor fragment. Nature 369, 160-163.  
912 10.1038/369160a0.

913 Strunk, T., Hamacher, K., Hoffgaard, F., Engelhardt, H., Zillig, M.D., Faist, K., Wenzel, W., and  
914 Pfeifer, F. (2011). Structural model of the gas vesicle protein GvpA and analysis of GvpA  
915 mutants in vivo. Mol Microbiol 81, 56-68. 10.1111/j.1365-2958.2011.07669.x.

916 Uldahl, K.B., Jensen, S.B., Bhoobalan-Chitty, Y., Martinez-Alvarez, L., Papathanasiou, P., and  
917 Peng, X. (2016). Life Cycle Characterization of Sulfolobus Monocaudavirus 1, an Extremophilic  
918 Spindle-Shaped Virus with Extracellular Tail Development. J Virol 90, 5693-5699.  
919 10.1128/JVI.00075-16.

920 Wang, F., Baquero, D.P., Su, Z., Beltran, L.C., Prangishvili, D., Krupovic, M., and Egelman, E.H.  
921 (2020). The structures of two archaeal type IV pili illuminate evolutionary relationships. *Nat.*  
922 *Commun.* *11*, 3424. 10.1038/s41467-020-17268-4.

923 Wang, F., Cvirkaite-Krupovic, V., Kreutzberger, M.A.B., Su, Z., de Oliveira, G.A.P., Osinski, T.,  
924 Sherman, N., DiMaio, F., Wall, J.S., Prangishvili, D., et al. (2019). An extensively glycosylated  
925 archaeal pilus survives extreme conditions. *Nat Microbiol* *4*, 1401-1410. 10.1038/s41564-019-  
926 0458-x.

927 Weber, M.S., Eibauer, M., Sivagurunathan, S., Magin, T.M., Goldman, R.D., and Medalia, O.  
928 (2021). Structural heterogeneity of cellular K5/K14 filaments as revealed by cryo-electron  
929 microscopy. *eLife* *10*. 10.7554/eLife.70307.

930 Williams, C.J., Headd, J.J., Moriarty, N.W., Prisant, M.G., Videau, L.L., Deis, L.N., Verma, V.,  
931 Keedy, D.A., Hintze, B.J., Chen, V.B., et al. (2018). MolProbity: More and better reference data  
932 for improved all-atom structure validation. *Protein Science* *27*, 293-315. 10.1002/pro.3330.

933 Winkler, H. (2007). 3D reconstruction and processing of volumetric data in cryo-electron  
934 tomography. *J. Struct. Biol.* *157*, 126-137. <https://doi.org/10.1016/j.jsb.2006.07.014>.

935 Xiang, X., Chen, L., Huang, X., Luo, Y., She, Q., and Huang, L. (2005). *Sulfolobus tengchongensis*  
936 spindle-shaped virus STSV1: virus-host interactions and genomic features. *J Virol* *79*, 8677-8686.  
937 10.1128/JVI.79.14.8677-8686.2005.

938 Zheng, S.Q., Palovcak, E., Armache, J.P., Verba, K.A., Cheng, Y., and Agard, D.A. (2017).  
939 MotionCor2: anisotropic correction of beam-induced motion for improved cryo-electron  
940 microscopy. *Nat. Methods* *14*, 331-332. 10.1038/nmeth.4193.

941 Zheng, W., Pena, A., Low, W.W., Wong, J.L.C., Frankel, G., and Egelman, E.H. (2020).  
942 Cryoelectron-Microscopic Structure of the pKpQIL Conjugative Pili from Carbapenem-Resistant  
943 *Klebsiella pneumoniae*. *Structure* *28*, 1321-1328 e1322. 10.1016/j.str.2020.08.010.

944 Zillig, W., Kletzin, A., Schleper, C., Holz, I., Janekovic, D., Hain, J., Lanzendörfer, M., and  
945 Kristjansson, J.K. (1993). Screening for Sulfolobales, their plasmids and their viruses in *Icelandic*  
946 *sofataras*. *Systematic and Applied Microbiology* *16*, 609-628.

947

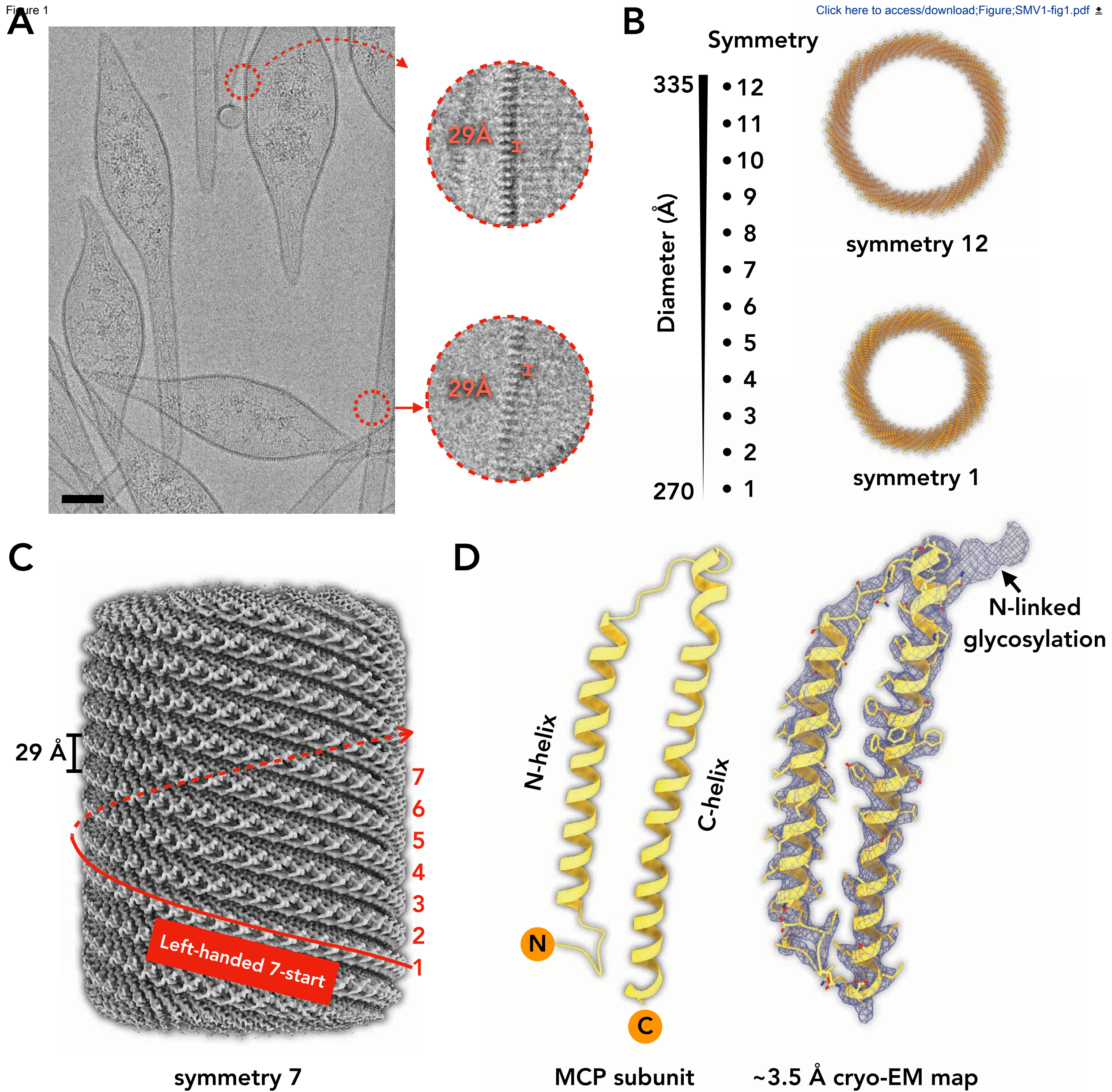
**TABLE FOR AUTHOR TO COMPLETE**

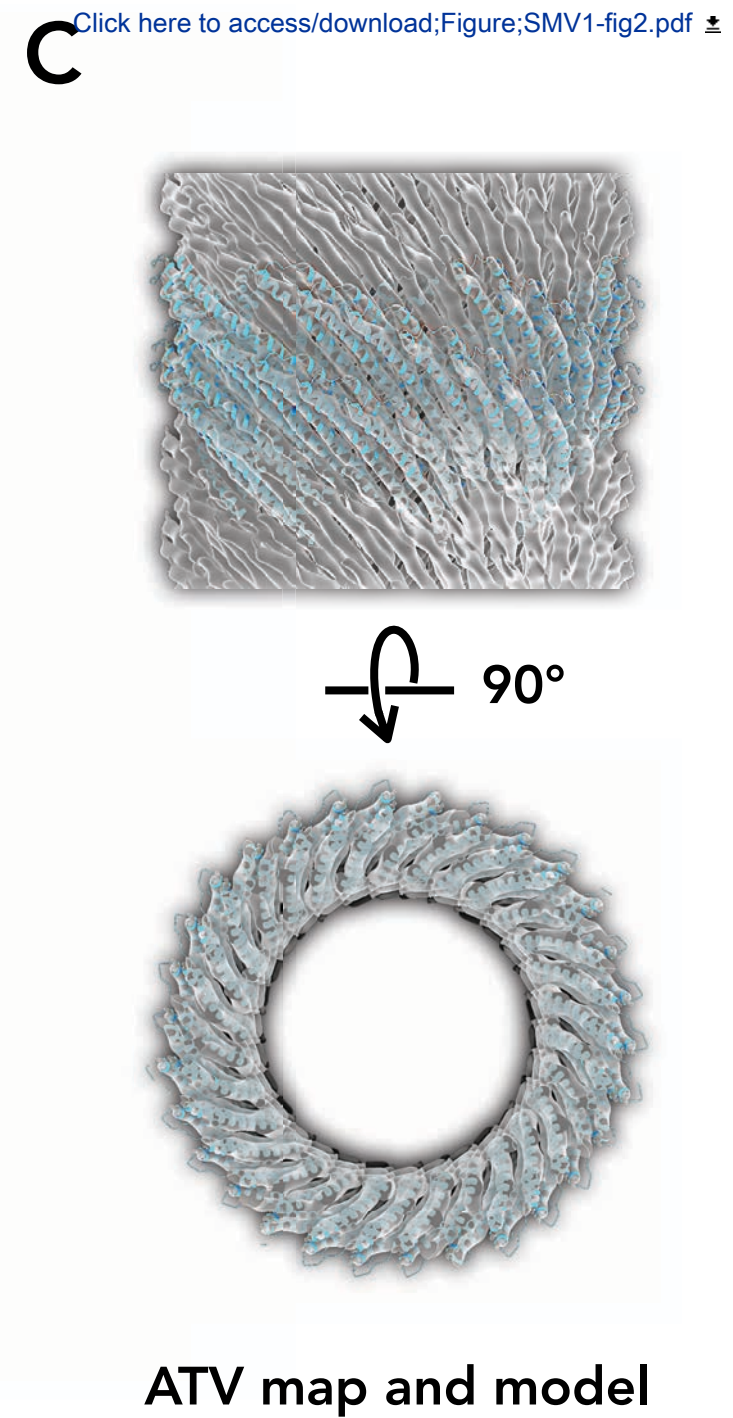
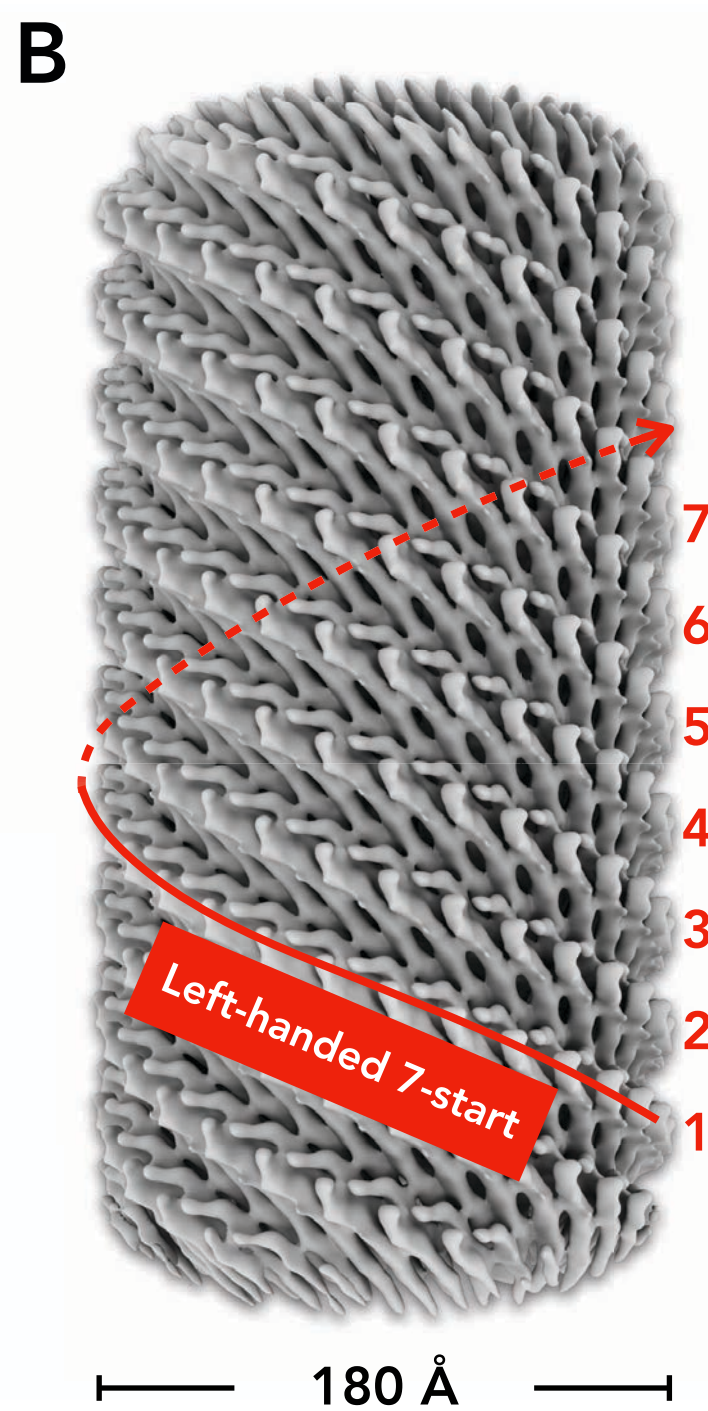
Please upload the completed table as a separate document. **Please do not add subheadings to the key resources table.** If you wish to make an entry that does not fall into one of the subheadings below, please contact your handling editor. **Any subheadings not relevant to your study can be skipped.** (NOTE: For authors publishing in *Cell Genomics*, *Cell Reports Medicine*, *Current Biology*, and *Med*, please note that references within the KRT should be in numbered style rather than Harvard.)

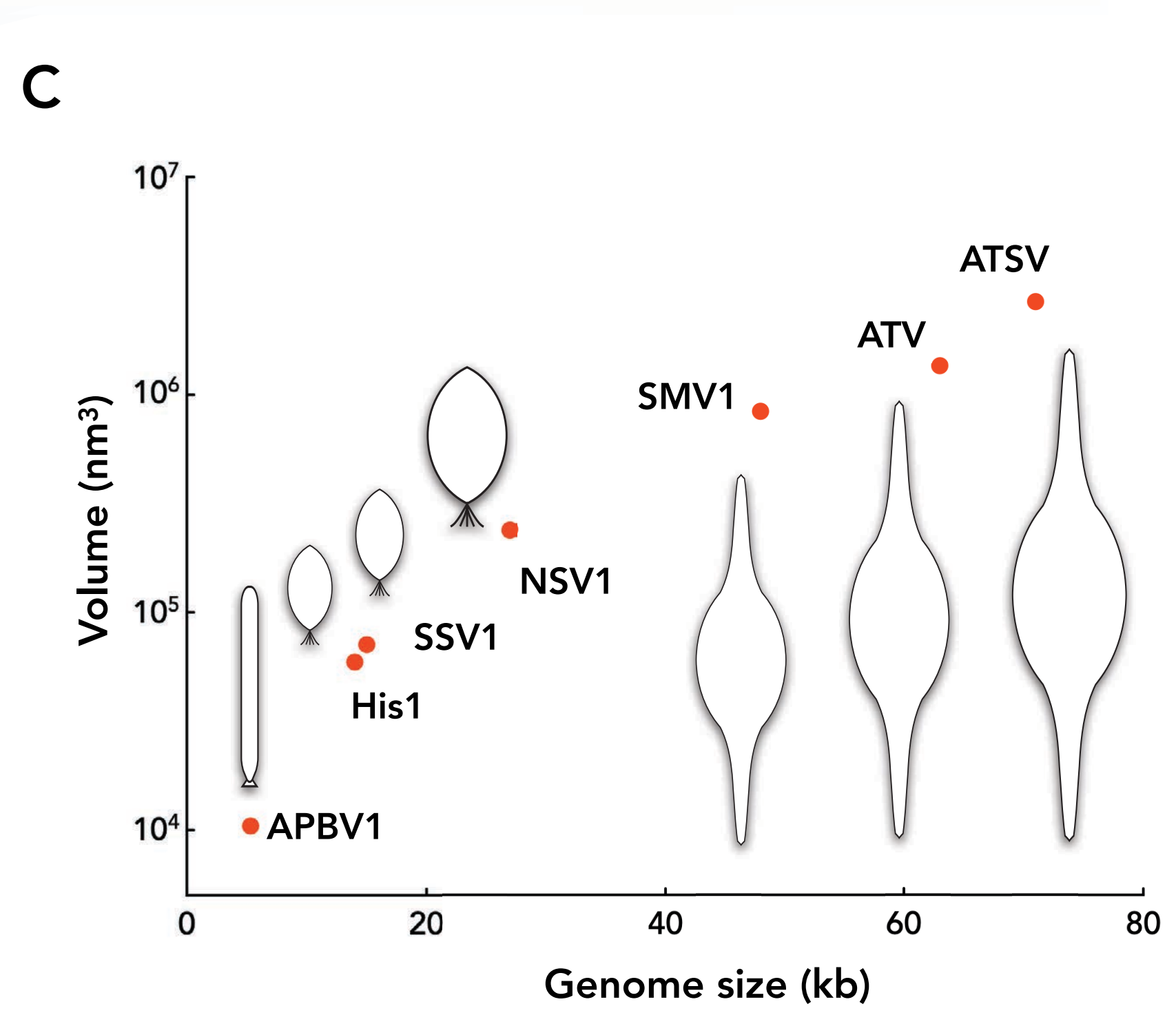
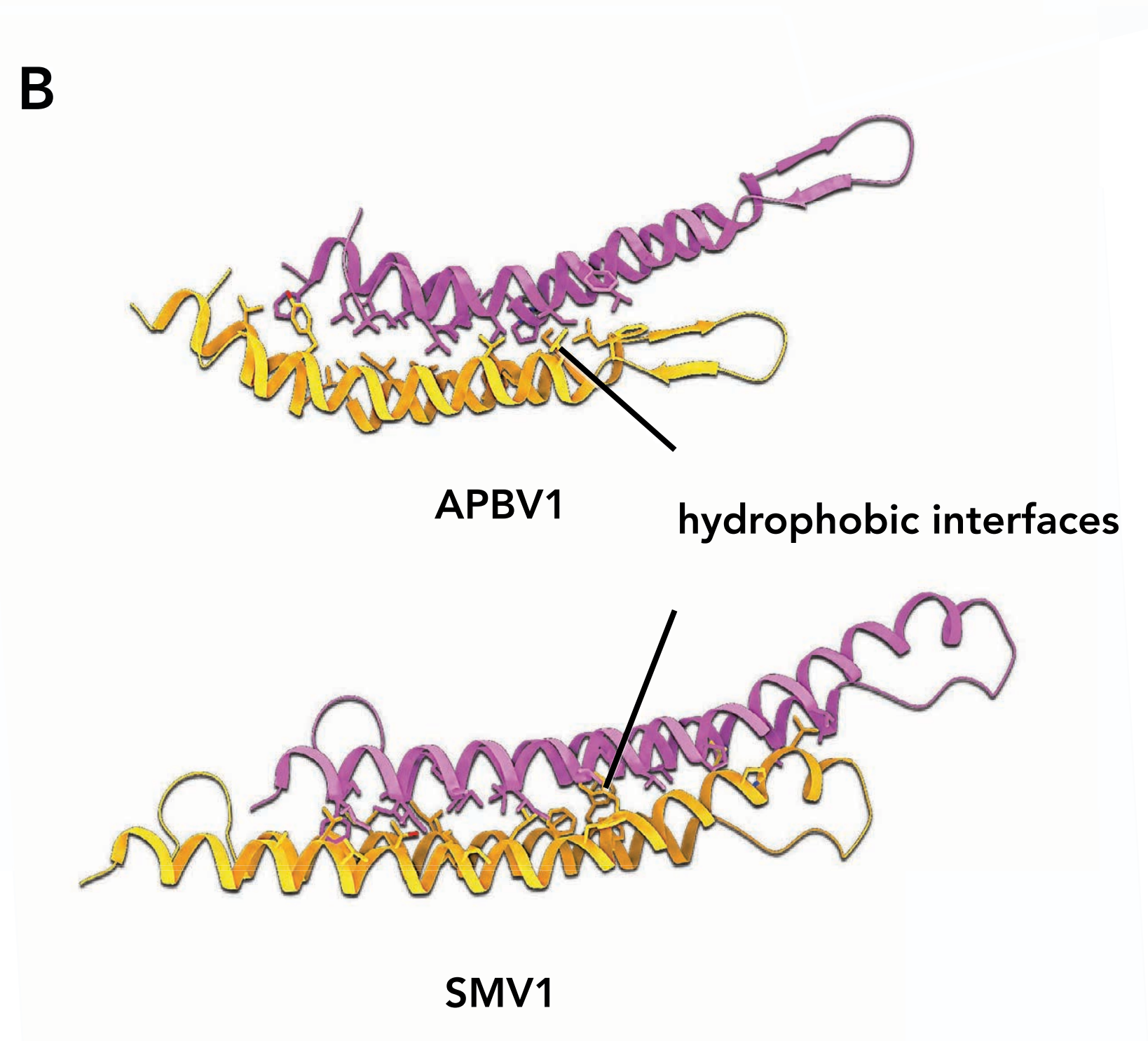
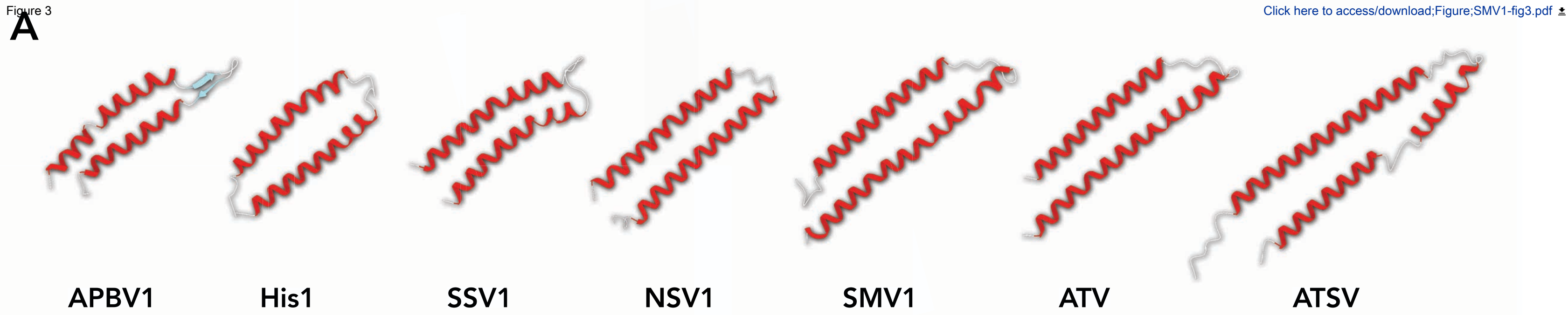
**Key resources table**

REAGENT or RESOURCE	SOURCE	IDENTIFIER
Archaeal and virus strains		
SMV1	Uldahl et al., 2016	N/A
ATV	Prangishvili et al., 2006	N/A
<i>Saccharolobus islandicus</i> ΔC1C2	Gudbergsdottir et al., 2011	N/A
<i>Acidianus covivator</i> AA9	Prangishvili et al., 2006	N/A
Chemicals, peptides, and recombinant proteins		
Bacto Tryptone	Gibco	Cat #: 211705
Bacto yeast extract	Gibco	Cat #: 212750
Sucrose	Sigma-Aldrich	Cat #: S0389
PEG6000	Sigma-Aldrich	Cat #: 81260
NaCl	Sigma-Aldrich	Cat #: S9888
Trisma base	Sigma-Aldrich	Cat #: T1503
Acetic acid	Sigma-Aldrich	Cat #: A6283
CsCl	Euromedex	Cat #: EU0770
Ethidium bromide	Eurobio Scientific	Cat #: GEPBET02-AF
InstantBlue	Abcam	Cat #: ab119211
Deposited data		

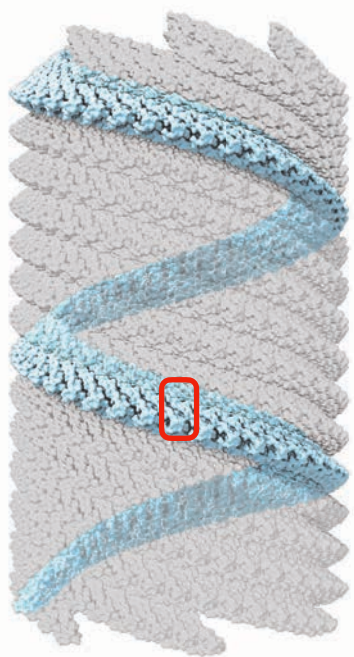
SMV1 Cryo-EM maps	This paper	EMDB: EMD-24585, EMD-24586, EMD-24587, EMD-24588, EMD-24589, EMD-24590, EMD-24591, EMD-24592, EMD-24593, EMD-24594, EMD-24595, EMD-24597
SMV1 Cryo-EM atomic models	This paper	PDB: 7RO2, 7RO3, 7RO4, 7RO5, 7RO6, 7ROB, 7ROC, 7ROD, 7ROE, 7ROG, 7ROH, 7ROI
ATV Cryo-EM map	This paper	EMDB: EMD-24596
Software and algorithms		
cryoSPARC	Punjani et al., 2017	<a href="https://cryosparc.com">https://cryosparc.com</a>
Chimera	Pettersen et al., 2004	<a href="https://www.cgl.ucsf.edu/chimera">https://www.cgl.ucsf.edu/chimera</a>
DeepTracer	Pfab et al., 2021	<a href="https://deepttracer.uw.edu">https://deepttracer.uw.edu</a>
Coot	Emsley and Cowtan, 2004	<a href="https://www2.mrc-lmb.cam.ac.uk/personal/pemsley/coot">https://www2.mrc-lmb.cam.ac.uk/personal/pemsley/coot</a>
Phenix	Afonine et al., 2018	<a href="https://phenix-online.org">https://phenix-online.org</a>
MolProbity	Williams et al., 2018	<a href="http://molprobity.biochem.duke.edu">http://molprobity.biochem.duke.edu</a>
Psi-Blast	Altschul et al., 1997	<a href="https://www.ebi.ac.uk/Tools/sss/psiblast/">https://www.ebi.ac.uk/Tools/sss/psiblast/</a>
PROMALS3D	Pei and Grishin, 2014	<a href="http://prodata.swmed.edu/promals3d/promals3d.php">http://prodata.swmed.edu/promals3d/promals3d.php</a>
AlphaFold2	Jumper et al., 2021	<a href="https://alphafold.ebi.ac.uk">https://alphafold.ebi.ac.uk</a>
FATCAT	Li et al., 2020	<a href="http://fatcat.godziklab.org/">http://fatcat.godziklab.org/</a>



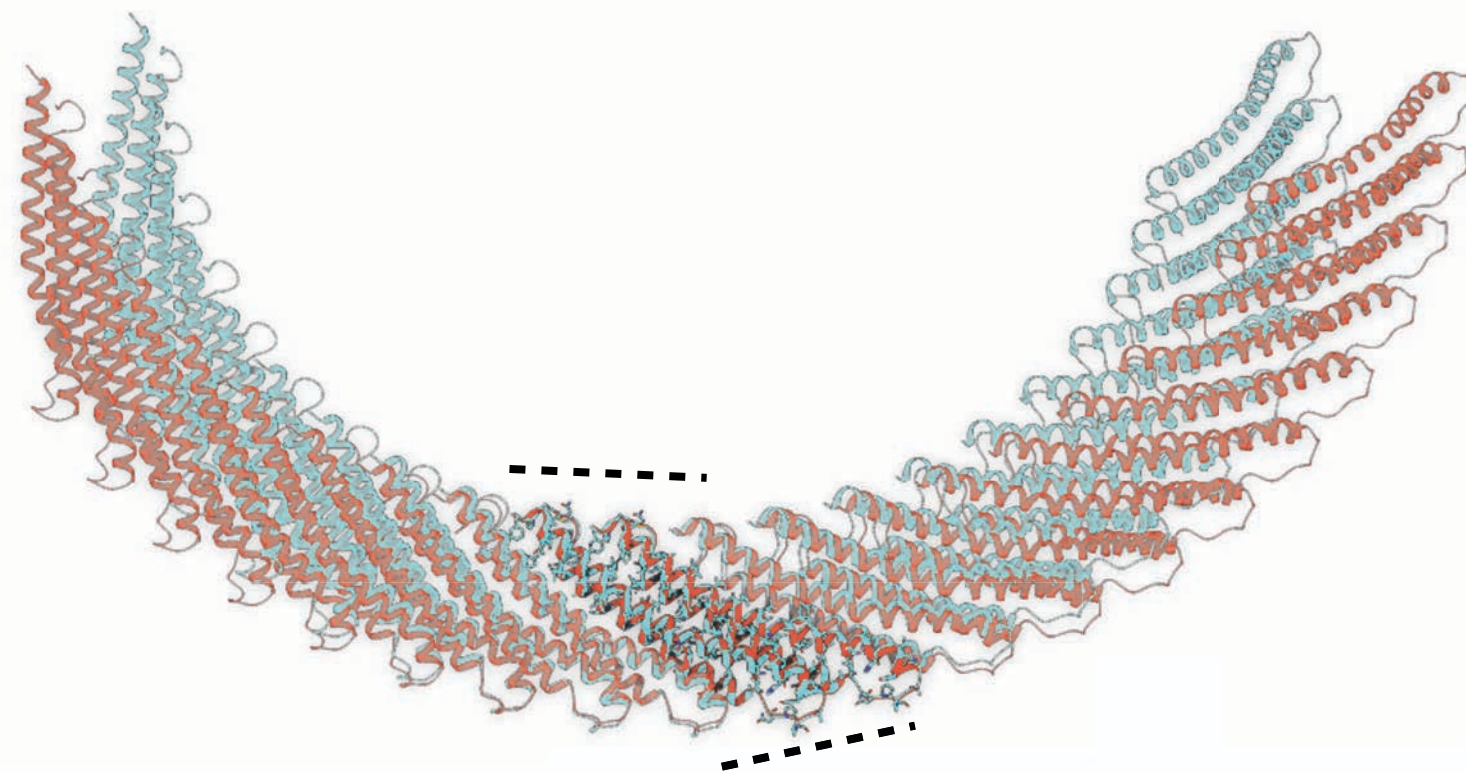




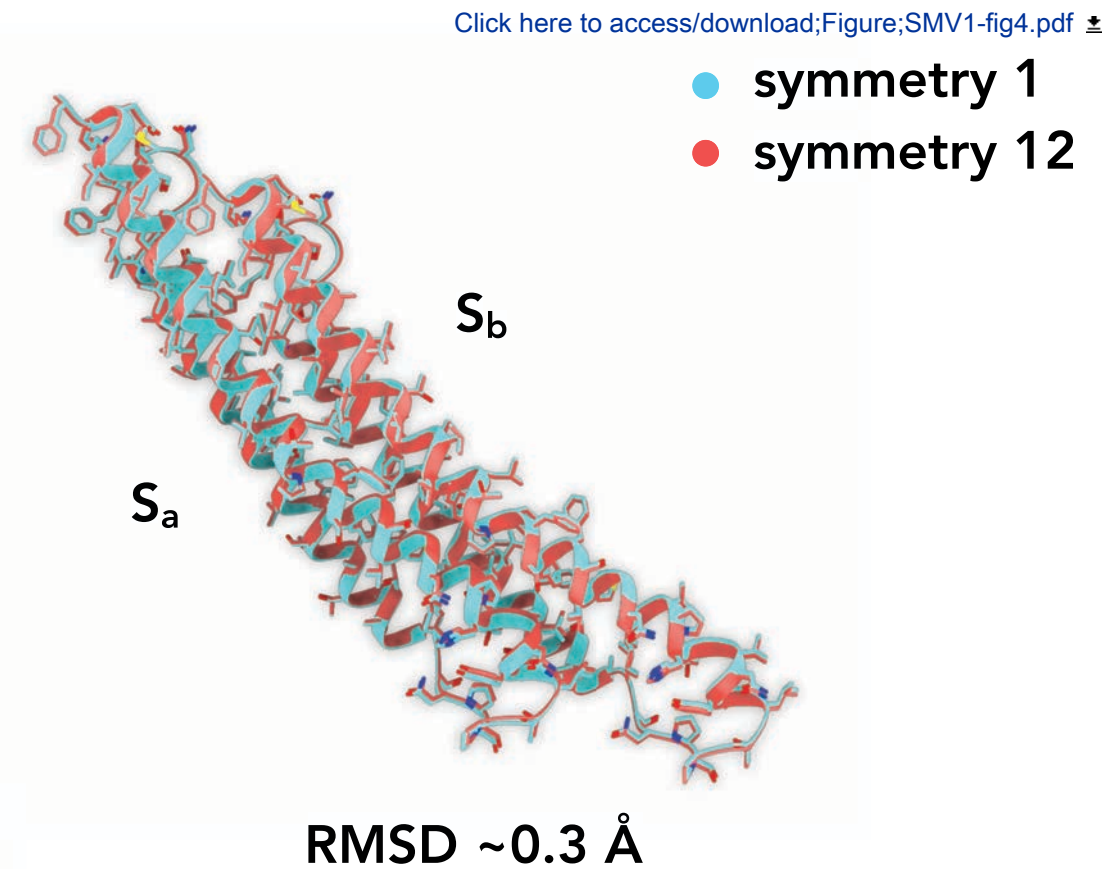
A



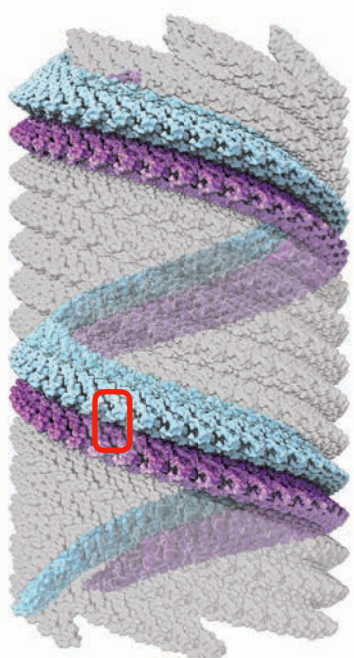
Interactions along the 7-start



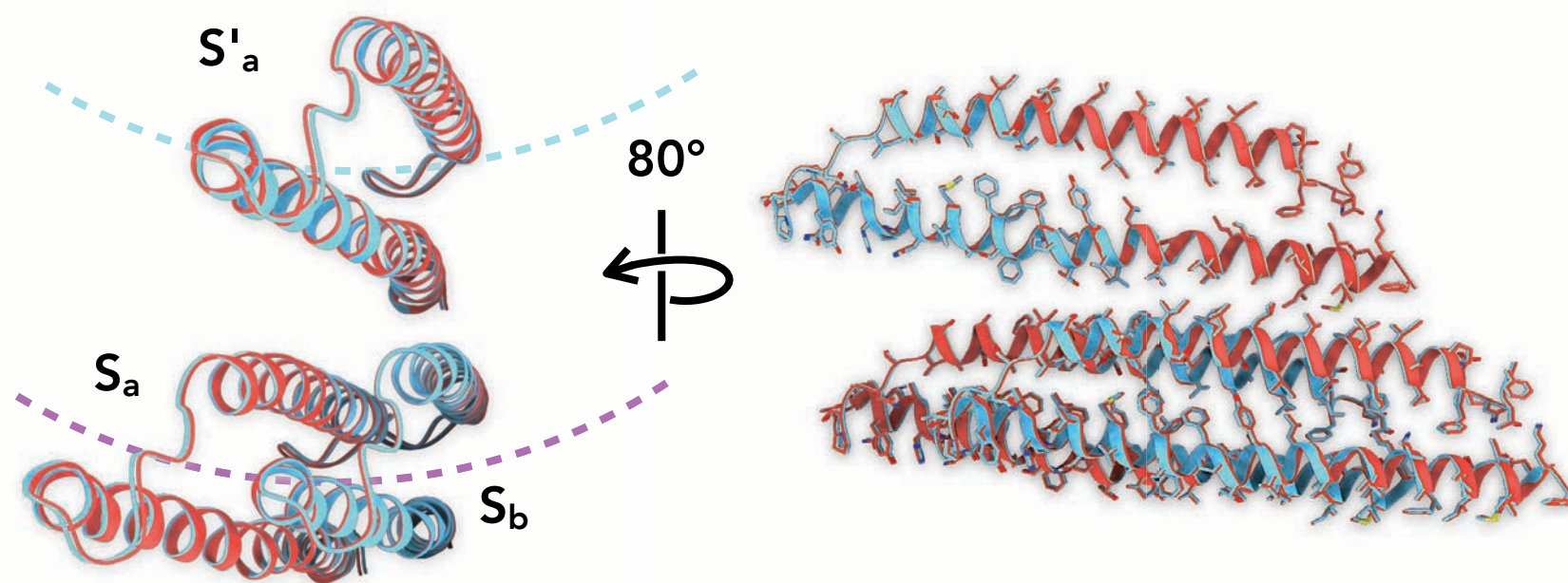
Aligned by two subunits



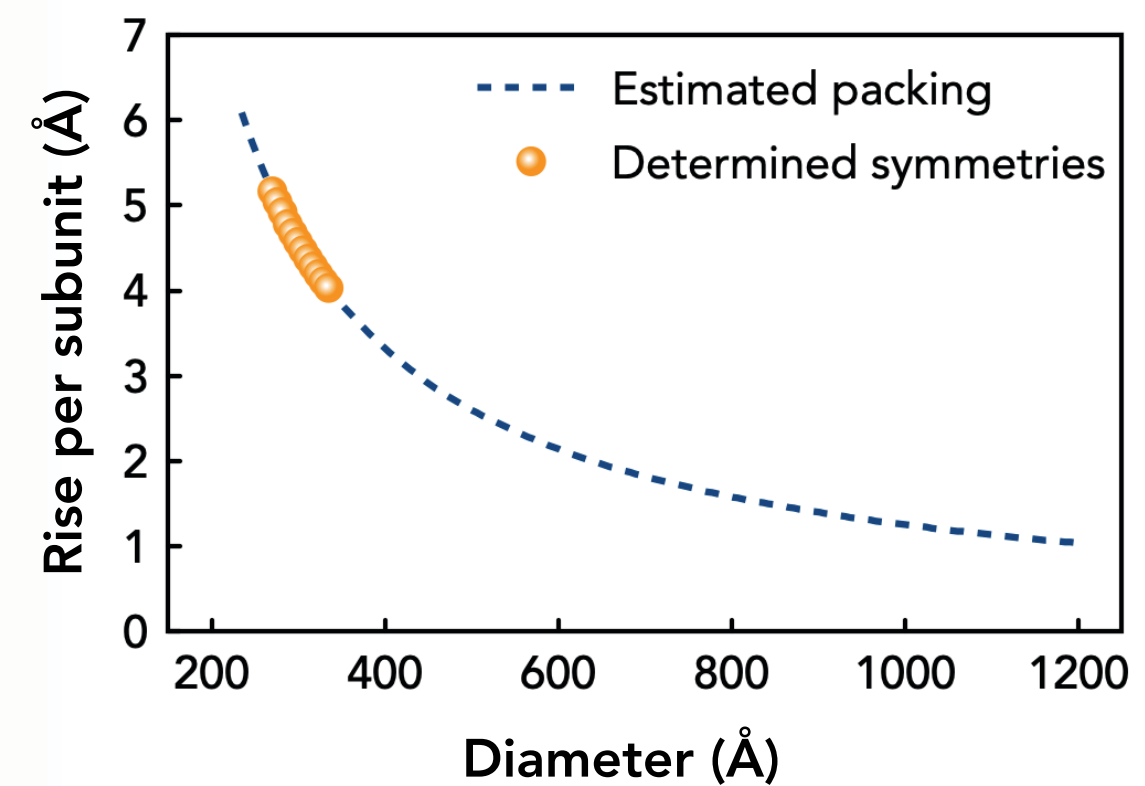
B

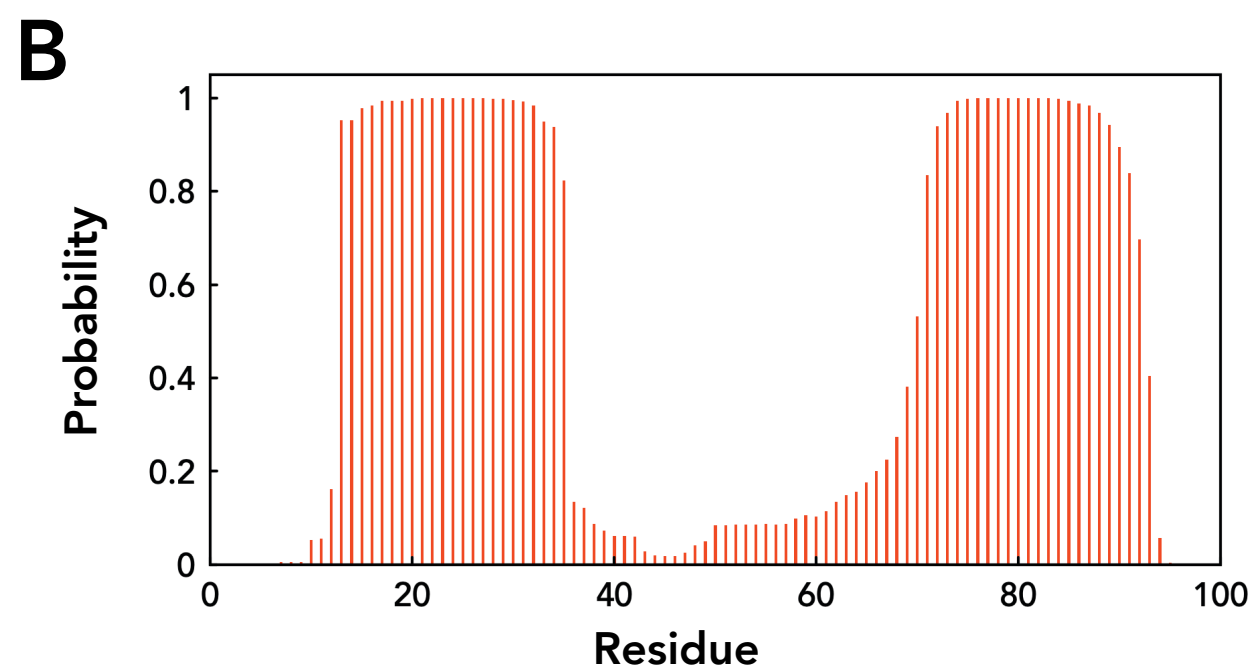
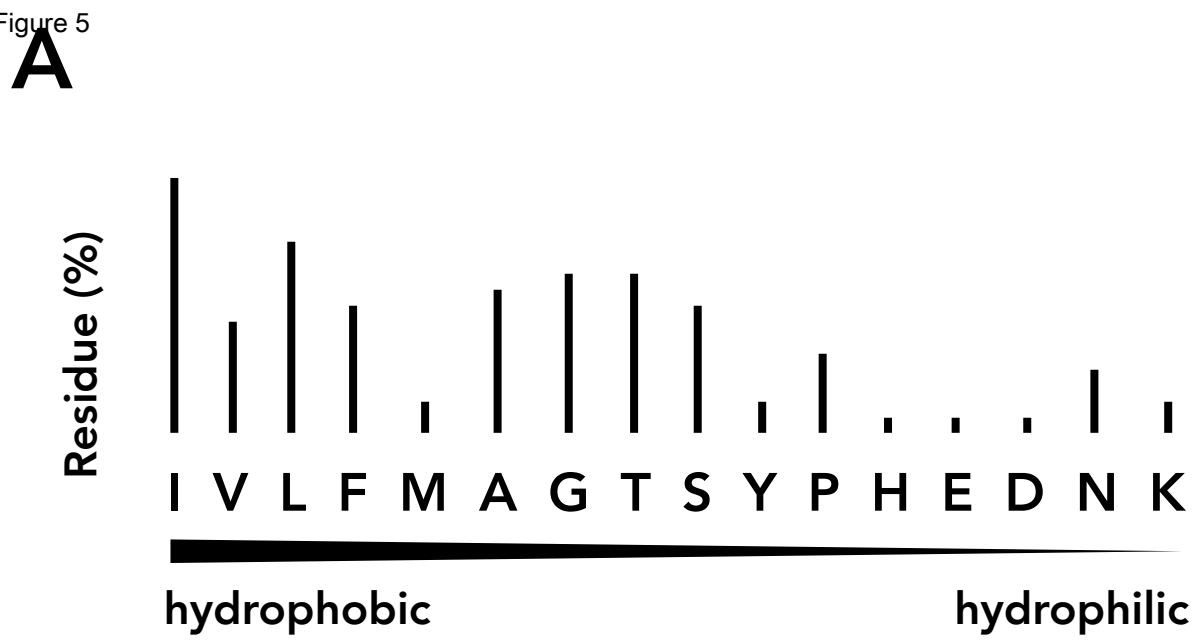


Interactions between 7-start protofilaments

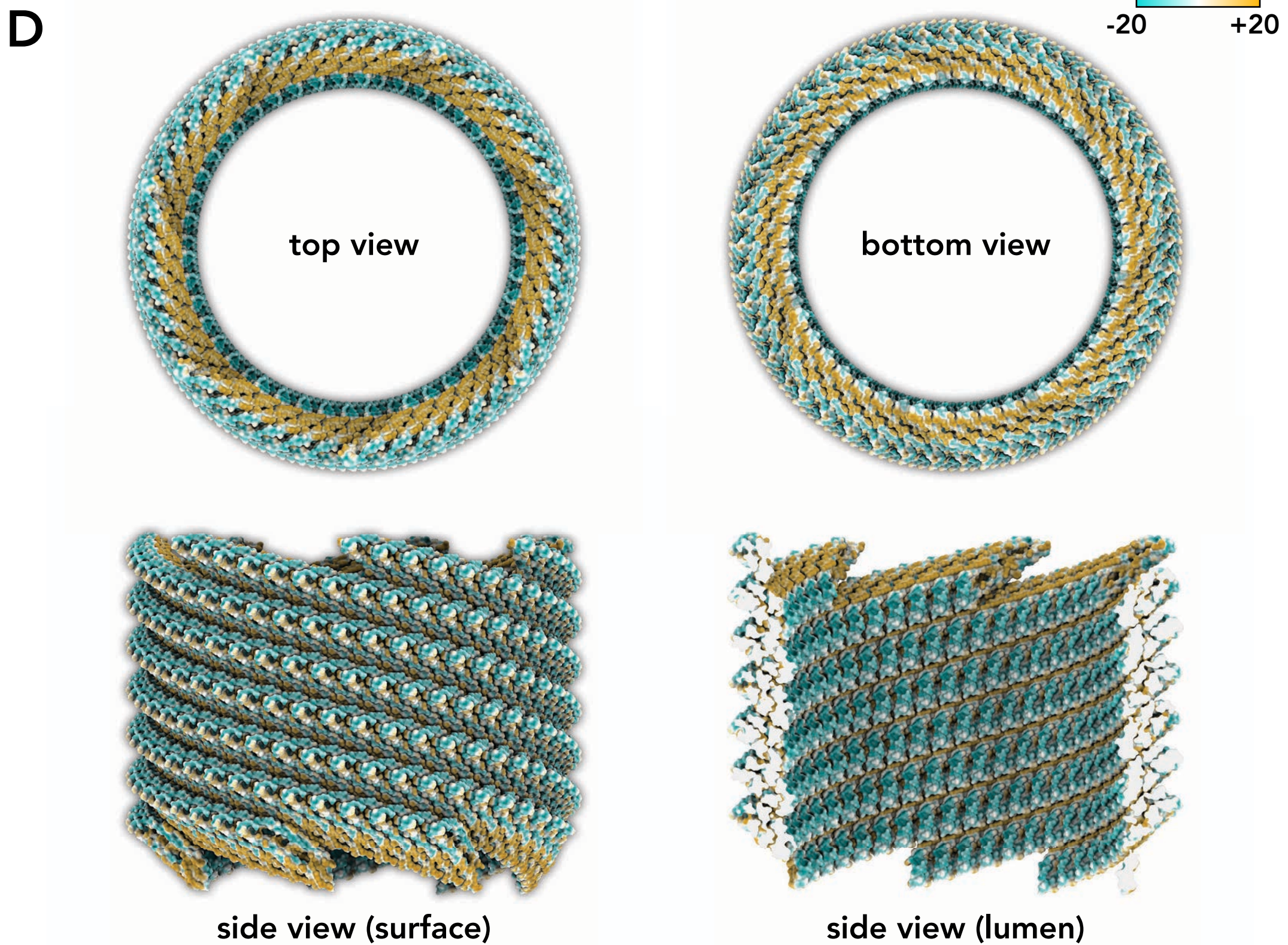
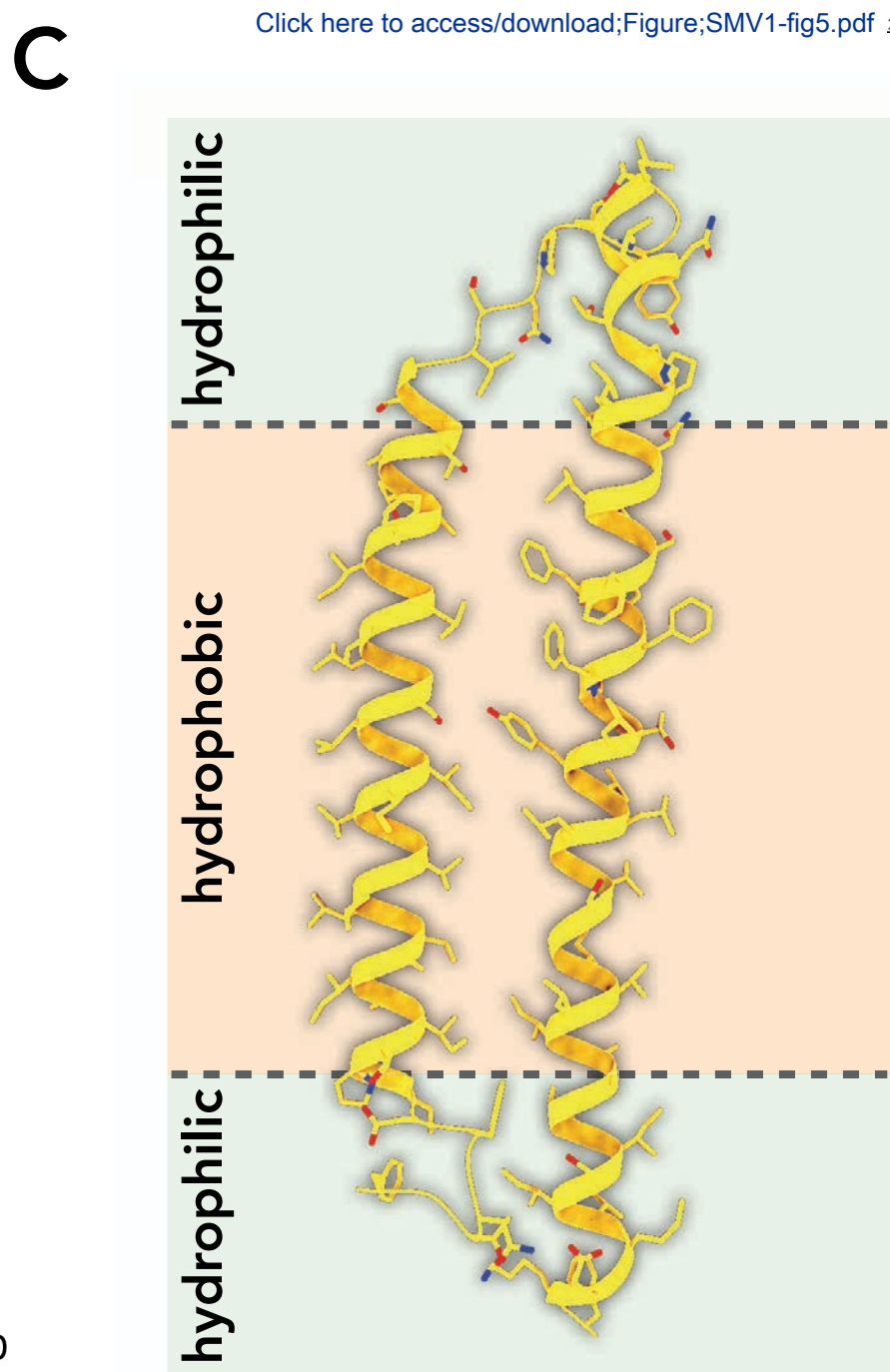
RMSD  $\sim 0.4$  Å

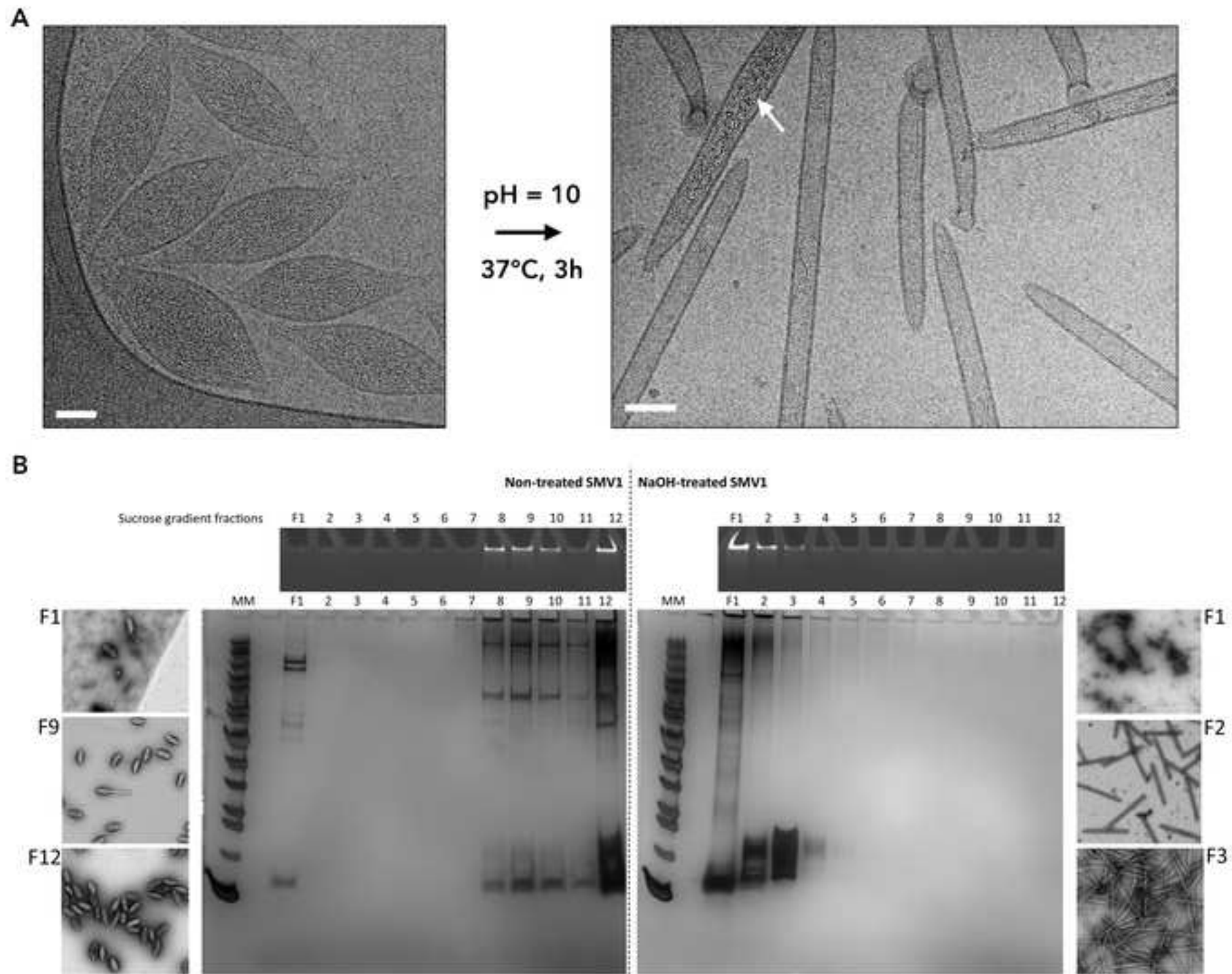
C

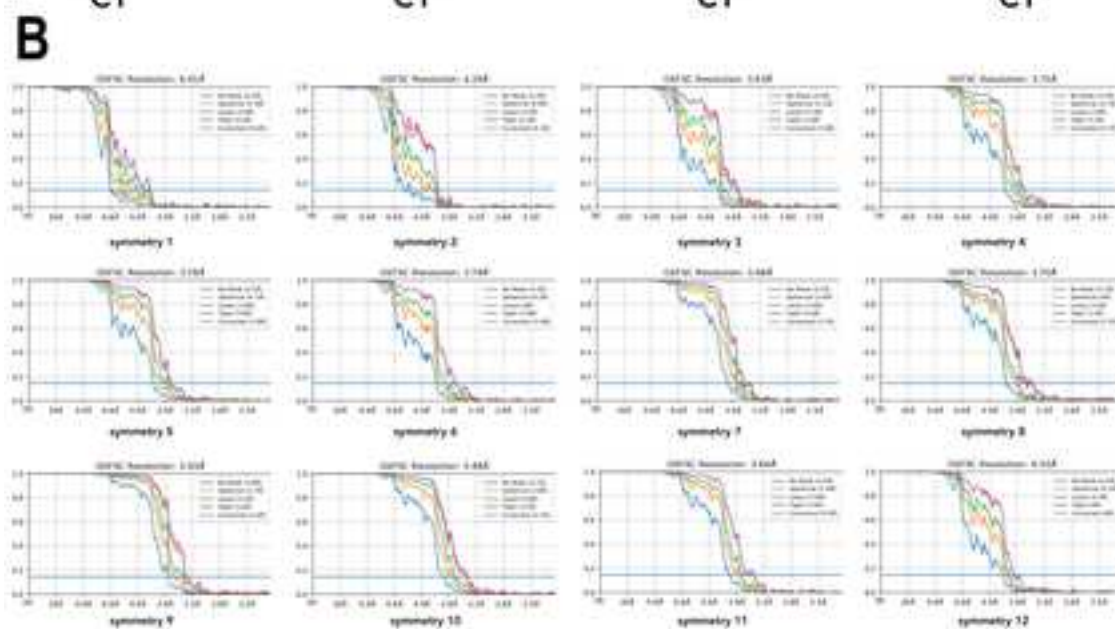
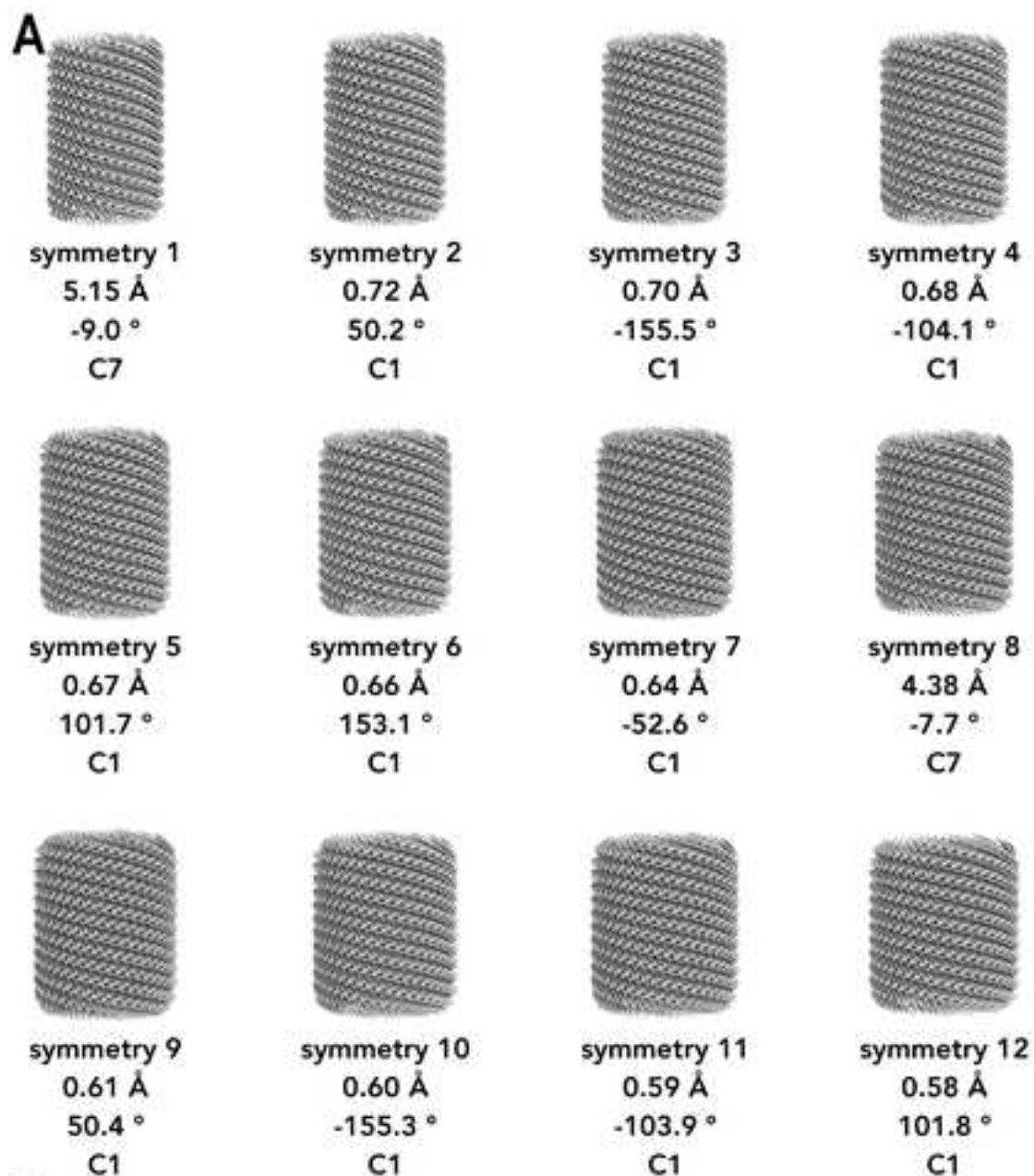


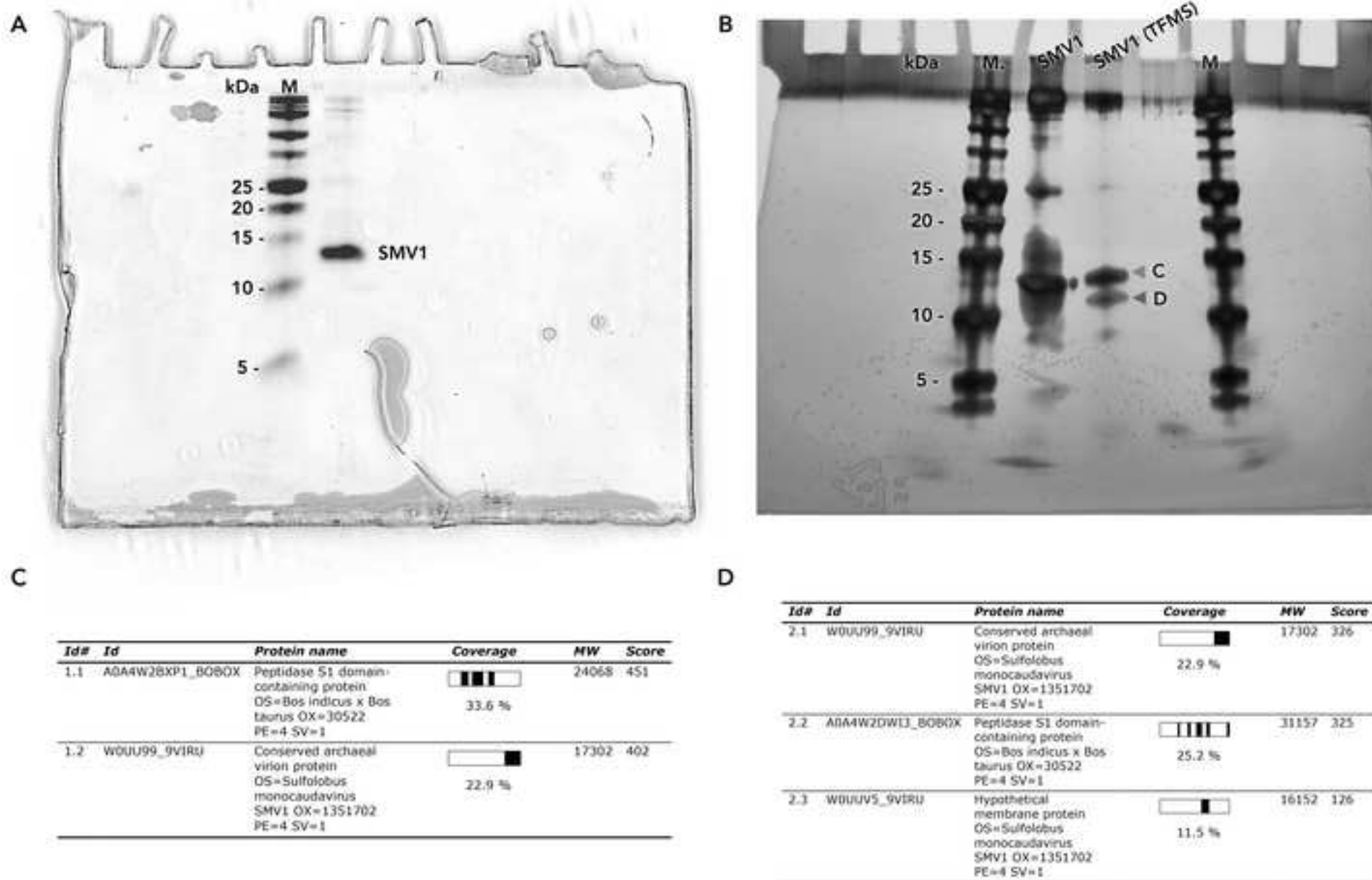


TMHMM transmembrane probabilities

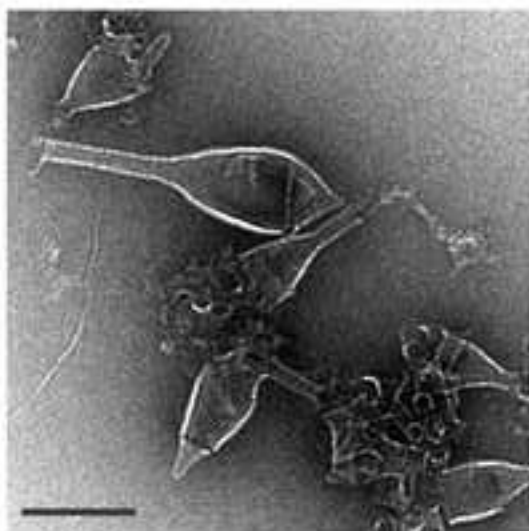










**A****B**